Journal of Computational Physics **164,** 283–334 (2000)
doi:10.1006/jcph.2000.6598, available online at http://www.idealibrary.com on IDEAL®

The MoT-ICE: A New High-Resolution Wave-Propagation Algorithm for Multidimensional Systems of Conservation Laws Based on Fey's Method of Transport

Sebastian Noelle[1]

Institut für Geometrie und Praktische Mathematik, RWTH Aachen, Templergraben 55, D-52056 Aachen, Germany
E-mail: noelle@igpm.rwth-aachen.de

Received August 31, 1999; revised February 28, 2000

Fey's Method of Transport (*MoT*) is a multidimensional flux-vector-splitting scheme for systems of conservation laws. Similarly to its one-dimensional forerunner, the Steger–Warming scheme, and several other upwind finite-difference schemes, the *MoT* suffers from an inconsistency at sonic points when used with piecewise-constant reconstructions. This inconsistency is due to a cell-centered evolution scheme, which we call *MoT-CCE*, that is used to propagate the waves resulting from the flux-vector-splitting step. Here we derive new first-order- and second-order-consistent characteristic schemes based on interface-centered evolution, which we call *MoT-ICE*. We prove consistency at all points, including the sonic points. Moreover, we simplify Fey's wave decomposition by distinguishing clearly between a linearization and a decomposition step. Numerical experiments confirm the stability and accuracy of the new schemes. Owing to the simplicity of the two new ingredients of the *MoT-ICE*, its second-order version is several times faster than that of the *MoT-CCE*.

Key Words: systems of conservation laws; multidimensional flux-vector splitting; Fey's Method of Tranport; interface-centered evolution.

CONTENTS

[1] Supported in part by Deutsche Forschungsgemeinschaft, DFG-SPP ANumE.

0021-9991/00 $35.00

1. INTRODUCTION

Since the work of Godunov [13], Van Leer [42], Harten–Lax [14], and Roe [35], the numerical solution of systems of hyperbolic conservation laws has been dominated by Riemann-solver-based schemes. This approach has been called flux-difference splitting, since the difference of two fluxes is decomposed into one-dimensional waves. These one-dimensional schemes are usually extended to several spatial dimensions either by using dimensional-splitting on Cartesian grids or by using the finite-volume approach on unstructured grids. For both approaches, convergence and error estimates have been established for multidimensional *scalar* conservation laws; see for example the results and references in [2, 4, 17, 28, 29, 41, 46]. Naturally, there are no comparable results for multidimensional *systems*, since no existence and uniqueness of the p.d.e.'s is known in this case.

The first systematic criticism of using one-dimensional Riemann solvers for multidimensional gasdynamics goes back to Roe himself [36]: the Riemann solver is applied in the grid rather than the flow direction, which may lead to a misinterpretation of the local wave structure of the solution. LeVeque and Walder [22] present difficulties of Godunov's scheme for strong two-dimensional shock waves arising in astrophysical flows and propose the use of rotated Riemann solvers. In [27, 37] Roe and Noelle study oscillations generated by dimensional-splitting schemes for a prototype linear system. A description of a number of failings of exact and approximate Riemann solvers for the two-dimensional Euler equations of gasdynamics, in particular the "odd–even decoupling" and the "carbuncle" phenomenon, may be found in Quirk's paper [34]. Recently, several authors have analyzed instabilities of one-dimensional flux-difference-splitting schemes for Quirk's examples (cf. [32, 47] and the references therein).

Since the mid 1985s, Roe, Deconinck, Van Leer, and many others have developed the so-called fluctuation-splitting schemes for the equations of gasdynamics (see [5, 44, 45]). Other multidimensional approaches include Colella's Corner-Transport-Upwind (CTU) scheme [3], LeVeque's CLAWPACK [18, 21], and the Weighted-Average-Flux (WAF) scheme of Billet and Toro [1].

In this paper we focus on Fey's Method of Transport (*MoT*) [7–11]. The *MoT* belongs to the family of flux-vector-splitting schemes first introduced by Sanders and Prendergast [39] and Steger and Warming [40]. Instead of decomposing the divergence of the flux vector, as in the fluctuation-splitting schemes of Roe *et al.*, one splits the conservative variables and the flux vector themselves. In the original version of Fey's *MoT* [7], the acoustic waves were integrated over the entire Mach cone in two dimensions, and hence the scheme could be interpreted as an Euler-Characteristic-Galerkin method (see [31] and [24] for recent related progress). Subsequently Fey, Jeltsch, and collaborators simplified the *MoT* and expanded it in various directions (see [8–11, 25, 26]).

The starting point of this work are the papers [9, 11]. In these papers, the *MoT* takes the following form: Step 1. A multidimensional wave model leads to a reformulation of the conservation law as a finite set of coupled nonlinear advection equations. Step 2. At the beginning of each timestep, the system is linearized and decomposed into a set of linear scalar advection equations with variable coefficients. Step 3. The solution of each linear advection equation at the end of the timestep is computed using a characteristic scheme. Step 4. The solution is projected back onto the conservative variables using the wave model of Step 1.

Our own contribution to Fey's method may be summarized as follows: Given a multidimensional wave model (Step 1), we simplify Step 2 by distinguishing clearly between the linearization and the decomposition step. This makes it possible to write down a general second-order-correction term for the decomposition error in a single line. Then we discuss the first-order version of Fey's characteristic scheme (Step 3) and show an inconsistency of the numerical scheme on the level of the linear advection equation. Subsequently, we derive new and particularly simple characteristic schemes based on piecewise-constant (respectively piecewise-linear) reconstructions and prove that they are uniformely first- (respectively second-order-) consistent. To apply these characteristic schemes to nonlinear systems of conservation laws, one needs to predict the solution at the interfaces between the cells of the computational domain at the half-timestep. At this stage we use flux-difference-splitting techniques to stabilize discontinuous solutions.

Owing to the simpler second-order-correction term for the decomposition error and the simplicity of the new characteristic scheme our second-order scheme is several times faster than Fey's scheme and seems to be competitive with state-of-the-art second-order algorithms.

Even though we only present numerical experiments in two spatial dimensions, it is possible and in fact straightforward to generalize our new scheme to the three-dimensional case (see the Remark following Definition 3.2, in particular Eq. (87)).

Fey's transport algorithm might be called *MoT-CCE*, since his advection scheme uses cell-centered evolution. We call our new scheme, which is based on interface centered evolution, *MoT-ICE*. When combined with piecewise-constant (respectively linear) reconstructions, we call the schemes *P0* (respectively *P1*).

The paper is organized as follows: In Section 2.1, we recall Fey's multidimensional wave models. In Section 2.2, we derive our second-order-accurate linearization and decomposition. In Section 3.1, we present a class of characteristic schemes for linear advection equations with variable coefficients. In Section 3.2, we show the inconsistency of the *MoT-ICE-P0*. In Section 3.3, we present the *MoT-ICE* and prove uniform first-order (respectively second-order) consistency of the *MoT-ICE-P0* (respectively *MoT-ICE-P1*). In Section 4, we generalize the method to systems of conservation laws. We give full details of first- and second-order-consistent algorithms in two spatial dimensions and prove their consistency. In Sections 5.1–5.5, we present numerical experiments. The comparison of cpu times is given in Section 5.6. In Section 6, we summarize our results.

Some of the results of this paper have been announced, but not proved, in [30].

2. DECOMPOSITION OF MULTIDIMENSIONAL SYSTEMS OF CONSERVATION LAWS INTO ADVECTION EQUATIONS

In this section, we recall Fey's advection form for multidimensional systems of conservation laws and give a general second-order-accurate linearization and decomposition of systems which can be written in advection form.

2.1. *A General Framework for Multidimensional Flux-Vector Splitting*

Consider a multidimensional system of m conservation laws in d spatial dimensions,

$$\partial_t \mathbf{U} + \nabla \cdot \underline{\mathbf{F}}(\mathbf{U}) = \mathbf{0}, \tag{1}$$

when $\mathbf{U}\colon \mathbb{R}^d \times \mathbb{R}_+ \to \mathcal{U} \subset \mathbb{R}^m$ is the state vector and $\underline{\mathbf{F}}\colon \mathcal{U} \to \mathbb{R}^{m\times d}$ is the flux. We will always denote column vectors in state space $\mathbb{R}^m$ by bold capital letters and row vectors in physical space $\mathbb{R}^d$ by underlined small letters. Note that the divergence acts on the rows of $\underline{\mathbf{F}} = (\mathbf{F}_1, \dots, \mathbf{F}_d)$.

EXAMPLE 2.1. We start our discussion with a very brief review of the Steger–Warming flux-vector splitting for the Euler equations of gasdynamics in one dimension. All we need to know at the moment about the Euler equations is that $\mathbf{F}(\mathbf{U})$ is homogeneous of degree 1 in $\mathbf{U}$, and so $\mathbf{F}(s\mathbf{U}) = s\mathbf{F}(\mathbf{U})$ for all real s. Differentiating with respect to s and evaluating at $s = 1$ gives

$$\mathbf{F}(\mathbf{U}) = \mathbf{F}'(s\mathbf{U})\mathbf{U}|_{s=1} = \mathbf{F}'(\mathbf{U})\mathbf{U}, \tag{2}$$

where $\mathbf{F}'$ is the Jacobian matrix of $\mathbf{F}$. Since the system is hyperbolic, $\mathbf{F}'(\mathbf{U})$ possesses m real eigenvalues $a_l(\mathbf{U})$ and a complete set of eigenvectors $\{\mathbf{R}_1(\mathbf{U}), \dots, \mathbf{R}_m(\mathbf{U})\}$, and so we may project $\mathbf{U}$ onto these eigenvectors,

$$\mathbf{U} = \sum_{l=1}^{m} s_l(\mathbf{U})\mathbf{R}_l(\mathbf{U}) =: \sum_{l=1}^{m} \mathbf{S}_l(\mathbf{U}). \tag{3}$$

Here $s_l(\mathbf{U})$ are uniquely defined real coefficients. From (2) and (3) we obtain

$$\mathbf{F}(\mathbf{U}) = F'(\mathbf{U}) \sum_{l=1}^{m} s_l(\mathbf{U})\mathbf{R}_l(\mathbf{U}) = \sum_{l=1}^{m} a_l(\mathbf{U})s_l(\mathbf{U})\mathbf{R}_l(\mathbf{U}) = \sum_{l=1}^{m} a_l(\mathbf{U})\mathbf{S}_l(\mathbf{U}). \tag{4}$$

Thus we can split both the state vector and the flux vector into m parts, $\mathbf{S}_l(\mathbf{U})$ and $a_l(\mathbf{U})\mathbf{S}_l(\mathbf{U})$, which we will call components in the following. Using this decomposition we rewrite the Euler equations as a sum of advection equations,

$$\sum_{l=1}^{m} (\partial_t \mathbf{S}_l(\mathbf{U}) + \partial_x (a_l(\mathbf{U})\mathbf{S}_l(\mathbf{U}))) = \mathbf{0}. \tag{5}$$

For a more detailed exposition as well as the definition of the Euler equations we refer the reader to [9, 40].

In [7, 8], Fey generalized the one-dimensional Steger–Warming splitting to the multi-dimensional Euler equations by integrating a set of suitably modified one-dimensional decompositions over all possible directions of propagation (e.g., the Mach cone for the acoustic waves). Ostkamp [31] showed that the resulting algorithm is closely related to an Euler Characteristic Galerkin method (compare also [24]). Since the integration over the Mach cone was computationally rather expensive, Fey, Jeltsch, and collaborators [9–11] went on and replaced the integration of the accoustic waves over the Mach cone by a sum over finitely many waves. In this way, they arrived at the following abstract framework for multidimensional flux-vector splitting:

DEFINITION 2.1. A *wave-model* for (1) is a set of $L \geq 1$ continuously differentiable mappings $\mathbf{S}_l \in \mathcal{C}^1(\mathcal{U}, \mathbb{R}^m)$ (called waves) and $\underline{a}_l \in C^1(\mathcal{U}, \mathbb{R}^d)$ (called advection velocities), $l = 1, \dots, L$, such that the following two consistency conditions are satisfied for all $\mathbf{U} \in \mathcal{U}$:

(i) consistency with the state vector,

$$\sum_{l=1}^{L} \mathbf{S}_l(\mathbf{U}) = \mathbf{U}, \tag{6}$$

(ii) consistency with the flux vector,

$$\sum_{l=1}^{L} \mathbf{S}_l(\mathbf{U})\underline{a}_l(\mathbf{U}) = \underline{\mathbf{F}}(\mathbf{U}). \tag{7}$$

Given a wave model, the conservation law (1) may be rewritten in the following *advection form*:

$$\sum_{l=1}^{L} (\partial_t \mathbf{S}_l(\mathbf{U}) + \nabla \cdot (\mathbf{S}_l(\mathbf{U})\underline{a}_l(\mathbf{U}))) = \mathbf{0}. \tag{8}$$

Thus we decompose the state vector $\mathbf{U}$ into L waves $\mathbf{S}_l(\mathbf{U})$, which are then transported with the advection velocities $\underline{a}_l(\mathbf{U})$. Motivated by the Steger–Warming splitting for the one-dimensional Euler equations, one may think of the waves $S_l(\mathbf{U})$ and the advection velocities $\underline{a}_l(\mathbf{U})$ as generalized eigenvectors and eigenvalues of the Jacobian matrices $\underline{\mathbf{F}}'(\mathbf{U})$.

Before we discuss how to use the advection form numerically, let us give some examples of multidimensional wave models.

EXAMPLE 2.2. Consider a hyperbolic system (1) with homogeneous flux

$$\underline{\mathbf{F}}(\mathbf{U}) = \underline{\mathcal{A}}(\mathbf{U})\mathbf{U} = (\mathcal{A}_1(\mathbf{U})\mathbf{U}, \ldots, \mathcal{A}_d(\mathbf{U})\mathbf{U}), \tag{9}$$

where

$$\mathcal{A}_j(\mathbf{U}) = \mathbf{F}'_j(\mathbf{U}), \quad j = 1 \ldots d, \tag{10}$$

are the Jacobians of the components of $\underline{\mathbf{F}}(U)$. We assume that the system is hyperbolic, so that each matrix $\mathcal{A}_j(\mathbf{U})$ is diagonalizable with real eigenvalues $a_{jl}(\mathbf{U}), l = 1, \ldots, m$. Furthermore, we even suppose that the $\mathcal{A}_j(\mathbf{U})$ are simultaneously diagonalizable (i.e., they commute). Then they have a *common* complete set of eigenvectors $\mathbf{R}_l(\mathbf{U}), l = 1, \ldots, m$.

Now we can split the state and the flux vector analogously to the Steger–Warming splitting: we project the state vector $\mathbf{U}$ onto the eigenvectors,

$$\mathbf{U} = \sum_{l=1}^{m} s_l(\mathbf{U})\mathbf{R}_l(\mathbf{U}) =: \sum_{l=1}^{m} \mathbf{S}_l(\mathbf{U}), \tag{11}$$

and immediately obtain the consistency relation (6). For the corresponding advection velocities we choose the lth eigenvalues of the matrices $\mathcal{A}_j(\mathbf{U})$,

$$\underline{a}_l(\mathbf{U}) = (a_{1l}(\mathbf{U}), \ldots, a_{dl}(\mathbf{U})), \tag{12}$$

and easily verify the consistency with the flux (7),

$$\begin{aligned}\sum_{l=1}^{m} \mathbf{S}_l(\mathbf{U})\underline{a}_l(\mathbf{U}) &= \sum_{l=1}^{m} (s_l(\mathbf{U})\mathbf{R}_l(\mathbf{U}))\underline{a}_l(\mathbf{U}) \\ &= \sum_{l=1}^{m} s_l(\mathbf{U})(a_{1l}(\mathbf{U})\mathbf{R}_l(\mathbf{U}), \dots, a_{dl}(\mathbf{U})\mathbf{R}_l(\mathbf{U})) \\ &= \sum_{l=1}^{m} s_l(\mathbf{U})(\mathcal{A}_1(\mathbf{U})\mathbf{R}_l(\mathbf{U}), \dots, \mathcal{A}_d(\mathbf{U})\mathbf{R}_l(\mathbf{U})) \\ &= \underline{\mathcal{A}}(\mathbf{U}) \left(\sum_{l=1}^{m} s_l(\mathbf{U})\mathbf{R}_l(\mathbf{U}) \right) \\ &= \underline{\mathcal{A}}(\mathbf{U})\mathbf{U} \\ &= \underline{\mathbf{F}}(\mathbf{U}). \end{aligned} \tag{13}$$

Note that if $\underline{\mathbf{F}}(\mathbf{U})$ is linear, we even have

$$\partial_t S_l(\mathbf{U}) + \nabla \cdot (S_l(\mathbf{U})\underline{a}_l) = \mathbf{R}_l[\partial_t s_l(\mathbf{U}) + \nabla \cdot (s_l(\mathbf{U})\underline{a}_l)] = \mathbf{0} \tag{14}$$

for each summand of (8) separately, which is the standard decomposition of a diagonalizable linear hyperbolic system into advection equations.

EXAMPLE 2.3. As an example of a nonhomogeneous system with noncommuting Jacobians, let us consider the equations of two-dimensional isentropic gasdynamics,

$$\begin{aligned} \rho_t + (\rho u)_x + (\rho v)_y &= 0 \\ (\rho u)_t + (\rho u^2 + \kappa\rho^\gamma)_x + (\rho uv)_y &= 0 \\ (\rho v)_t + (\rho uv)_x + (\rho v^2 + \kappa\rho^\gamma)_y &= 0 \end{aligned} \tag{15}$$

with $\kappa > 0$ and $\gamma \geq 1$, where ρ is the mass density, $\underline{u} = (u, v)$ is the velocity vector, and the sound velocity c is given by

$$c := (\gamma\kappa\rho^{\gamma-1})^{1/2}. \tag{16}$$

Now we may write

$$\mathbf{U} = \rho \begin{pmatrix} 1 \\ \underline{u}^T \end{pmatrix}, \qquad \underline{\mathbf{F}}(\mathbf{U}) = \mathbf{U}\underline{u} + \frac{\rho c^2}{\gamma} \begin{pmatrix} \underline{0} \\ \underline{\underline{I}} \end{pmatrix}, \tag{17}$$

where $\underline{0} = (0, 0)$ and $\underline{\underline{I}}$ is the 2×2 unit matrix. Note that $\rho c^2/\gamma$ is the pressure. Following Fey's work [9] on the nonisentropic Euler equations, Morel [26] gives the following splitting:

LEMMA 2.1. *For $L \in \mathbf{N}$ let $\underline{n}_l \in \mathbb{R}^2$, $l = 1, \dots, L$, be vectors satisfying*

$$\sum_{l=1}^{L} \underline{n}_l = \underline{0} \tag{18}$$

$$\frac{1}{L} \sum_{l=1}^{L} \underline{n}_l^T \underline{n}_l = \underline{\underline{I}}. \tag{19}$$

Here $\underline{n}_l^T \underline{n}_l = \underline{n}_l \otimes \underline{n}_l$ *denotes the tensor product. Then the waves*

$$\mathbf{S}_l(\mathbf{U}) := \frac{1}{L}\mathbf{U} + \frac{\rho c}{L\gamma}\begin{pmatrix} 0 \\ \underline{n}_l^T \end{pmatrix} \tag{20}$$

and advection velocities

$$\underline{a}_l(\mathbf{U}) := \underline{u} + c\underline{n}_l \tag{21}$$

satisfy the consistency relations (6) *and* (7).

The proof follows immediately from (17), (18), and (19).

As a particular case, one may choose $L = 4$ and

$$\underline{n}_l \in \{(1, 1), (1, -1), (-1, 1), (-1, -1)\} \tag{22}$$

(this is the choice in [9, 26], and we will use this choice in the numerical experiments in Section 5). In this case the components $a_{1l}(\mathbf{U})$ and $a_{2l}(\mathbf{U})$ of the advection velocities coincide with the eigenvalues $u \pm c$ and $v \pm c$, and we may interpret the waves as acoustic waves.

Note that if all the $\underline{n}_l$ have the same length, then (19) implies that $|\underline{n}_l| = \sqrt{2}$, and $|\underline{n}_l| = \sqrt{d}$ in d spatial dimensions. However, if the $\underline{n}_l$ were unit vectors, then the $\mathbf{S}_l(\mathbf{U})$ and $\underline{a}_l(\mathbf{U})$ would coincide with the eigenvectors and physical speeds of propagation in the direction $\underline{n}_l$ as naturally happens in the one-dimensional situation. In this case, however, condition (19) and hence (7) would be violated. One can also rule out this inconsistent choice using the following heuristic stability argument: Let us compare the choice of $\underline{n}_l$ in (22) with the alternative choice

$$\underline{n}_l \in \{\sqrt{0.5}(1, 1), \sqrt{0.5}(1, -1), \sqrt{0.5}(-1, 1), \sqrt{0.5}(-1, -1)\} \tag{23}$$

(so $|\underline{n}_l| = 1$ in the latter case). Following the stability argument of Courant–Friedrichs–Lewy, we see that the domain of influence of the wave model should certainly contain that of the conservation law. We will see that this is true if the $\underline{n}_l$ are chosen by (22) but violated if they are chosen by (23) (see Fig. 1).

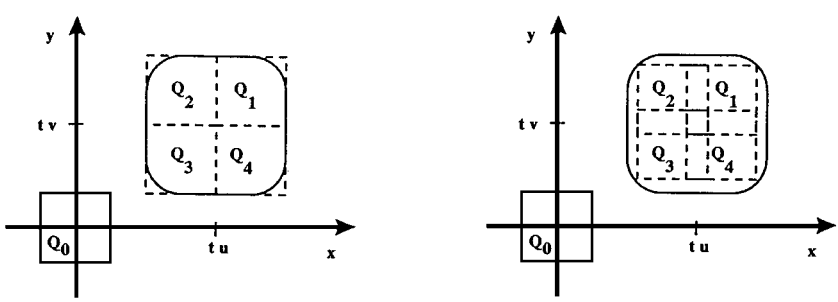

FIG. 1. The square Q_0, its domain of influence according to the conservation law (rounded square in solid lines, centered at $t(u, v)$), and the domain of influence of the wave model, which is the union of the four squares $Q_1, \ldots, Q_4$ (broken lines). Left: $|\underline{n}_l| = \sqrt{2}$. Right: $|\underline{n}_l| = 1$ (note that in this case, $Q_1, \ldots, Q_4$, all of which are translations of Q_0, overlap).

So suppose that data are given in some axiparallel square Q_0 with corners $(-r, -r)$, (r, r). The domain of influence of the linearized isentropic Euler equations is the set of all points which are contained in the Mach cone emanating from Q_0, i.e., the union of all disks of radius tc and with centers in $Q_0 + t(u, v)$. This is the square with rounded corners centered at $t(u, v)$, shown by a solid line in both figures. Let us denote this by M. Suppose now that for the wave model, we have constant waves $\mathbf{S}_l$ and advection velocities $\underline{a}_l$ and transport each wave in the direction $\underline{a}_l$ for some time t, such that $tc \le r$. Then the domain of influence of the square Q_0 (according to the wave model) will be the union of the four axiparallel squares $Q_l = Q_0 + t\underline{a}_l$, $l = 1, \dots, 4$. Let us denote this union by $\bar{Q} = \bigcup_{l=1}^{4} Q_l$. In the first case ($|\underline{n}_l| = \sqrt{2}$; left figure), $\bar{Q}$ coincides with the smallest axi parallel square which contains M, while in the second case ($|\underline{n}_l| = 1$; right figure) $\bar{Q}$ is strictly smaller than M and hence the wave model may be unstable.

We would also like to recall from [9] that one may modify the wave models of Lemma 2.1 using instead the waves

$$\mathbf{S}_l(\mathbf{U}) := \frac{1}{L}\mathbf{U} + \nu \frac{\rho c}{L\gamma} \begin{pmatrix} 0 \\ \underline{n}_l^T \end{pmatrix} \tag{24}$$

and advection velocities

$$\underline{a}_l(\mathbf{U}) := \underline{u} + \frac{c}{\nu}\underline{n}_l \tag{25}$$

for any nonzero $\nu \in \mathbb{R}$. Note that this wave model allows arbitrary advection velocities. Consistency is verified immediately for all ν, but the above stability consideration should be used to determine physically reasonable choices of the velocities.

It is well known that the equations of multidimensional gasdynamics cannot be diagonalized simultaneously. Therefore, we cannot expect the summands of (8) to be zero individually. To see this, we set

$$\begin{aligned} \partial_t \mathbf{S}_l(\mathbf{U}) + \nabla \cdot (\mathbf{S}_l(\mathbf{U})\underline{a}_l(\mathbf{U})) &= -\mathbf{S}_l'(\mathbf{U})\nabla \cdot \underline{\mathbf{F}}(\mathbf{U}) + \nabla \cdot (\mathbf{S}_l(\mathbf{U})\underline{a}_l(\mathbf{U})) \\ &=: \mathbf{T}_l(\mathbf{U}, \nabla\mathbf{U}), \end{aligned} \tag{26}$$

where $'$ denotes differentiation with respect to $\mathbf{U}$ and we have used the conservation law (1) to replace time by space derivatives. From (8), we see that

$$\sum_{l=1}^{L} \mathbf{T}_l(\mathbf{U}, \nabla\mathbf{U}) = \mathbf{0} \tag{27}$$

if $\mathbf{U}$ solves the conservation law. As a side remark, we note that this holds for any smooth function $\mathbf{U}$,

$$\begin{aligned} \sum_{l=1}^{L} \mathbf{T}_l(\mathbf{U}, \nabla\mathbf{U}) &= \sum_{l=1}^{L} (-\mathbf{S}_l(\mathbf{U})'\nabla \cdot \underline{\mathbf{F}}(\mathbf{U}) + \nabla \cdot (\mathbf{S}_l(\mathbf{U})\underline{a}_l(\mathbf{U}))) \\ &= \mathbf{U}'\nabla \cdot \underline{\mathbf{F}}(\mathbf{U}) - \nabla \cdot \underline{\mathbf{F}}(\mathbf{U}) = \mathbf{0}, \end{aligned}$$

since $\mathbf{U}'$ is the identity matrix in $\mathbb{R}^{m\times m}$.

Now we use (17), (20), (21), (25), and the notation $\underline{n}_l = (\alpha_l, \beta_l)$ and obtain after a tedious computation

$$\mathbf{T}_l = \frac{c\rho_x}{L}\begin{pmatrix} \frac{\gamma+1}{2}\alpha_l \\ \frac{\gamma+1}{2}u\alpha_l + \left(\alpha_l^2 - 1\right)c \\ \frac{\gamma+1}{2}v\alpha_l + \alpha_l\beta_l c \end{pmatrix} + \frac{c\rho u_x}{L}\begin{pmatrix} 0 \\ \frac{\gamma+1}{2\gamma}\alpha_l \\ \frac{\gamma-1}{2\gamma}\beta_l \end{pmatrix} + \frac{c\rho v_x}{L}\begin{pmatrix} 0 \\ 0 \\ \alpha_l \end{pmatrix}$$
$$+ \frac{c\rho_y}{L}\begin{pmatrix} \frac{\gamma+1}{2}\beta_l \\ \frac{\gamma+1}{2}u\beta_l + \alpha_l\beta_l c \\ \frac{\gamma+1}{2}v\beta_l + \left(\beta_l^2 - 1\right)c \end{pmatrix} + \frac{c\rho u_y}{L}\begin{pmatrix} 0 \\ \beta_l \\ 0 \end{pmatrix} + \frac{c\rho v_y}{L}\begin{pmatrix} 0 \\ \frac{\gamma-1}{2\gamma}\alpha_l \\ \frac{\gamma+1}{2\gamma}\beta_l \end{pmatrix}. \quad (28)$$

One can see immediately that this is in general nonzero. We will use these $\mathbf{T}_l$ in our numerical experiments for the shallow-water equations in Section 5.

Examples of wave models for other conservation laws, including the wave equation, the Euler equations, and the equations of ideal magnetohydrodynamics, may be found in [11]. Common to all of them is a finite set of acoustic waves which approximate the Mach cone (typically four waves in two spatial dimensions). For the Euler equations one adds an entropy wave, and for the MHD equations, one adds the two Alfvén and possibly some slow magneto-acoustic waves. We refer the reader to [9, 11] for a more detailed discussion.

For the equations of gasdynamics, wave models may be derived systematically from a kinetic formulation by replacing the Maxwellian distribution function by a sum of Dirac masses (see [48]).

We remark that the wave models presented here are fundamentally different from those introduced in the context of fluctuation-splitting schemes by Roe, Deconinck, and others (see [5, 36] and references therein). In the context of fluctuation-splitting schemes, the divergence of the flux vector, $\nabla \cdot \underline{\mathbf{F}}(\mathbf{U})$, is split into waves, while here the state vector $\mathbf{U}$ and flux vector $\underline{\mathbf{F}}(\mathbf{U})$ themselves (and not their derivatives) are decomposed. This is the crucial difference between flux-difference- and flux-vector-splitting schemes.

From now on, we assume that a system of conservation laws and a wave model consistent with that system in the sense of Definition 2.1 have already been chosen.

2.2. *Decomposition into Advection Equations*

Let us now see how the advection form (8) can be used when solving the initial value problem (1) with data $\mathbf{U}$ given at time $t_n = nk$, where $k = \Delta t$ is the timestep. Our aim is to develop algorithms which are *second-order accurate* in time and space for smooth solutions and are nonoscillatory at discontinuities. For the rest of this section, we assume that the solution $\mathbf{U}$ is smooth. Hence our accuracy requirement means that after a single timestep, at time $t_{n+1} = t_n + k$, the difference between the exact and the approximate solution should be of $\mathcal{O}(k^{2+1})$.

First we consider a linear, diagonalizable hyperbolic system (see Example 2.2 above). All one needs to do in this case is to solve the $L = m$ scalar equations (14), which can be done exactly. For general systems, this approach encounters two difficulties: first, in general the advection velocities $\underline{a}_l(\mathbf{U})$ depend on the solution itself; so they are not known in advance. Second, as we have proved for the equations of isentropic gasdynamics, we cannot expect that each summand $\mathbf{T}_l(\mathbf{U}, \nabla\mathbf{U})$ occuring in (8) is equal to zero individually. Recall that $\mathbf{T}_l(\mathbf{U}, \nabla\mathbf{U})$ was defined in (25).

In [9], Fey freezes the advection velocities at the original timestep t_n and then solves each component of (8) separately (with frozen velocities). Thus he has to solve $L \geq m$ linear advection equations, now with spatially varying coefficients. At the end of the timestep, the approximate solution is obtained as the sum over the L waves. This procedure leads to first-order in time linearization and decomposition errors, which are then removed by a suitable modification of the initial data to obtain a second-order in time linearization and decomposition. Zimmermann [48] points out that for the equations of gasdynamics this procedure is analogous to certain kinetic schemes [6, 33], where the collisionless Boltzmann equation is solved during one timestep, and then the solution is projected onto the corresponding equilibrium states by integrating (summing) the velocity distribution function. For kinetic schemes, the technique to modify the initial data to obtain second-order accuracy in time has been proposed by Deshpande [6].

We now study the linearization and decomposition errors separately and propose a slightly modified linearization and decomposition. Our next lemma shows that freezing the velocity field at the half-timestep $t_{n+1/2} = t_n + k/2$ gives a second-order-accurate linearization. We denote the frozen advection velocities by $\underline{\tilde{a}}_l$ and the solution of the linearized system by $\mathbf{V}$.

LEMMA 2.2 (Linearization). *Let* $\mathbf{U}$ *be a smooth solution of* (1), $k = \Delta t > 0$. *Let*

$$\mathbf{V}\colon \mathbb{R}^d \times [t_n, t_n + k] \to \mathbb{R}^m$$

be the solution of the initial value problem

$$\partial_t \mathbf{V} + \nabla \cdot \sum_{l=1}^{m} (\mathbf{S}_l(\mathbf{V}) \underline{\tilde{a}}_l) = \mathbf{0} \tag{29}$$

$$\mathbf{V}(t_n) = \mathbf{U}(t_n), \tag{30}$$

where the auxiliary velocity fields $\underline{\tilde{a}}_l\colon \mathbb{R}^d \to \mathbb{R}^d$, $l = 1, \ldots, L$, *satisfy*

$$\underline{\tilde{a}}_l(\underline{x}) = \underline{a}_l\left(\mathbf{U}\left(\underline{x}, t_n + \frac{k}{2}\right)\right) + \mathcal{O}(k^2). \tag{31}$$

Then

$$\mathbf{V}(t_n + k) - \mathbf{U}(t_n + k) = \mathcal{O}(k^3). \tag{32}$$

Note that the approximate transport velocities $\underline{\tilde{a}}_l$ are now *prescribed* coefficients which depend on space but not on time. In practice, they will have to be evaluated by a predictor step at the half-timestep $t_{n+1/2}$; see Section 4. System (29) is still *nonlinear* in $\mathbf{V}$. It is, however, *linear* in the components $\mathbf{S}_l(\mathbf{V})$, since

$$\partial_t \mathbf{V} - \sum_{l=1}^{L} \partial_t \mathbf{S}_l(\mathbf{V}).$$

This will become clear once we have decomposed (29) into its components; see (33) and (38) below.

Proof. The proof follows by expanding the solutions $\mathbf{V}$ of (29), (30) and $\mathbf{U}$ of (8) into Taylor series with respect to time. At $t = t_n$ we compute

$$\begin{aligned}
\mathbf{U}_t &= -\nabla \cdot \underline{\mathbf{F}}(\mathbf{U}) = -\nabla \cdot \sum \mathbf{S}_l(\mathbf{U})\underline{a}_l(\mathbf{U}) \\
\mathbf{U}_{tt} &= -\nabla \cdot \sum (\mathbf{S}_l'(\mathbf{U})\mathbf{U}_t\underline{a}_l(\mathbf{U}) + \mathbf{S}_l(\mathbf{U})\underline{a}_l(\mathbf{U})_t) \\
\mathbf{V}_t &= -\nabla \cdot \sum \mathbf{S}_l(\mathbf{V})\tilde{\underline{a}}_l \\
\mathbf{V}_{tt} &= -\nabla \cdot \sum \mathbf{S}_l'(\mathbf{V})\mathbf{V}_t\tilde{\underline{a}}_l = -\nabla \cdot \sum (\mathbf{S}_l'(\mathbf{V})\mathbf{V}_t\underline{a}_l(\mathbf{U})) + \mathcal{O}(k).
\end{aligned}$$

Therefore, using (31) and $\tilde{\underline{a}}_l(\underline{x}) = \underline{a}_l(\mathbf{U}(\underline{x}, t_n)) + \frac{k}{2}\partial_t \underline{a}_l(\mathbf{U}(\underline{x}, t_n)) + \mathcal{O}(k^2)$ we obtain

$$\begin{aligned}
\mathbf{V}_t - \mathbf{U}_t &= -\nabla \cdot \sum \mathbf{S}_l(\mathbf{U})(\tilde{\underline{a}} - \underline{a}_l(\mathbf{U})) = -\nabla \cdot \sum \mathbf{S}_l(\mathbf{U})\frac{k}{2}\underline{a}_l(\mathbf{U})_t + \mathcal{O}(k^2) \\
\mathbf{V}_{tt} - \mathbf{U}_{tt} &= -\nabla \cdot \sum (\mathbf{S}_l'(\mathbf{U})(\mathbf{V}_t - \mathbf{U}_t)\underline{a}_l(\mathbf{U}) - \mathbf{S}_l(\mathbf{U})\underline{a}_l(\mathbf{U})_t) + \mathcal{O}(k) \\
&= \nabla \cdot \sum \mathbf{S}_l(\mathbf{U})\underline{a}_l(\mathbf{U})_t + \mathcal{O}(k).
\end{aligned}$$

It follows that

$$\begin{aligned}
\mathbf{V}(t_n + k) - \mathbf{U}(t_n + k) &= (\mathbf{V} - \mathbf{U}) + k(\mathbf{V}_t + \mathbf{U}_t) + \frac{1}{2}k^2(\mathbf{V}_{tt} - \mathbf{U}_{tt}) + \mathcal{O}(k^3) \\
&= -\frac{1}{2}k^2\nabla \cdot \sum \mathbf{S}_l(\mathbf{U})\underline{a}_l(\mathbf{U})_t + \frac{1}{2}k^2\nabla \cdot \sum \mathbf{S}_l(\mathbf{U})\underline{a}_l(\mathbf{U})_t + \mathcal{O}(k^3) \\
&= \mathcal{O}(k^3). \quad \blacksquare
\end{aligned}$$

As a corollary to the proof, we note that if we had frozen the velocity field at the beginning of the timestep ($t = t_n$), then the linearization would have been only first-order accurate in time. Our linearization corresponds to integrating $\partial_t U = -\nabla \cdot \sum \mathbf{S}_l(\mathbf{U})\underline{a}_l(\mathbf{U})$ from time t_n to t_{n+1} using the midpoint rule in time for the advection velocities $\underline{a}_l(\mathbf{U})$ and exact integration for the waves $\mathbf{S}_l(\mathbf{U})$.

Next we consider the decomposition error. First, we simply decompose the linearized advection form (29) by setting each summand to zero separately, denoting the solution of the resulting system by $\mathbf{W}$ and its components by $\mathbf{W}_l$,

$$\mathbf{W} := \sum_{l=1}^{L} \mathbf{W}_l \colon \mathbb{R}^d \times [t_n, t_n + k] \to \mathbb{R}^m.$$

Now we suppose that each $\mathbf{W}_l$ solves the linear initial value problem

$$\partial_t \mathbf{W}_l + \nabla \cdot (\mathbf{W}_l\tilde{\underline{a}}_l) = \mathbf{0} \tag{33}$$

$$\mathbf{W}_l(t_n) = \mathbf{S}_l(\mathbf{U}(t_n)) = \mathbf{S}_l(\mathbf{V}(t_n)). \tag{34}$$

Then at time $t = t_n$

$$\begin{aligned}
\mathbf{W}_t - \mathbf{V}_t &= \mathbf{0} \\
\mathbf{W}_{tt} - \mathbf{V}_{tt} &= -\nabla \cdot \sum ((\mathbf{W}_l)_t - \mathbf{S}_l'(\mathbf{V})\mathbf{V}_t)\tilde{\underline{a}}_l \\
&= \nabla \cdot \sum \left(\nabla \cdot (\mathbf{W}_l\tilde{\underline{a}}_l) - \mathbf{S}_l'(\mathbf{V})\nabla \cdot \left(\sum \mathbf{S}_k(\mathbf{V})\tilde{\underline{a}}_k\right)\right)\tilde{\underline{a}}_l
\end{aligned}$$

$$
\begin{aligned}
&= \nabla \cdot \sum (\nabla \cdot (\mathbf{S}_l(\mathbf{U})\underline{a}_l(\mathbf{U})) - \mathbf{S}_l'(\mathbf{U})\nabla \cdot \underline{\mathbf{F}}(\mathbf{U}))\tilde{\underline{a}}_l + \mathcal{O}(k) \\
&= \nabla \cdot \sum (\nabla \cdot (\mathbf{S}_l(\mathbf{U})\underline{a}_l(\mathbf{U})) + \mathbf{S}_l'(\mathbf{U})\mathbf{U}_t)\tilde{\underline{a}}_l + \mathcal{O}(k) \\
&= \nabla \cdot \sum (\mathbf{S}_l(\mathbf{U})_t + \nabla \cdot (\mathbf{S})_l(\mathbf{U})\underline{a}_l(\mathbf{U})))\tilde{\underline{a}}_l + \mathcal{O}(k) \\
&= \nabla \cdot \sum T_l(\mathbf{U}, \nabla\mathbf{U})\tilde{\underline{a}}_l + \mathcal{O}(k),
\end{aligned}
$$

where we have used the definition (25) of $T_l(\mathbf{U}, \nabla\mathbf{U})$. Therefore

$$
\mathbf{W}(t_n + k) - \mathbf{V}(t_n + k) = \frac{k^2}{2}\nabla \cdot \sum_{l=1}^{L} \mathbf{T}_l(\mathbf{U}, \nabla\mathbf{U})\tilde{\underline{a}}_l + \mathcal{O}(k^3). \tag{35}
$$

We now modify the initial data of $\mathbf{W}$ to obtain a second-order-accurate linearization and decomposition. The most straightforward modification, replacing $\mathbf{W}(t_n)$ by

$$
\mathbf{U}(t_n) + \frac{k^2}{2}\nabla \cdot \sum_{l=1}^{L} \mathbf{T}_l(\mathbf{U}, \nabla\mathbf{U})\tilde{\underline{a}}_l,
$$

would require computing second numerical derivatives of the conservative variables. Even worse, it would violate the conservation principle. The same criticism applies if we replace the initial data for each component $\mathbf{W}_l(t_n)$ by

$$
\mathbf{S}_l(\mathbf{U}(t_n)) + \frac{k^2}{2}\nabla \cdot (\mathbf{T}_l(\mathbf{U}, \nabla\mathbf{U})\tilde{\underline{a}}_l).
$$

Instead, we replace $\mathbf{W}_l(t_n)$ by

$$
\mathbf{S}_l(\mathbf{U}(t_n)) + \frac{k}{2}\mathbf{T}_l(\mathbf{U}(t_n), \nabla\mathbf{U}(t_n)). \tag{36}
$$

Then we do not need to compute second derivatives, and conservation is guaranteed since by (27), $\sum \mathbf{T}_l(\mathbf{U}(t_n), \nabla\mathbf{U}(t_n)) = \mathbf{0}$, and so

$$
\sum_{l=1}^{L} \left(\mathbf{S}_l(\mathbf{U}(t_n)) + \frac{k}{2}\mathbf{T}_l(\mathbf{U}(t_n), \nabla\mathbf{U}(t_n)) \right) = \mathbf{U}(t_n). \tag{37}
$$

In the following theorem, we prove that this modification of the initial data indeed gives second-order accuracy. The crucial point is that it leads to a modified first derivative of the approximate solution. We denote the solution of the modified problem by $\mathbf{Z}$ and its components by $\mathbf{Z}_l$.

THEOREM 2.1 (Second-Order-Accurate Decomposition). *Let*

$$
\mathbf{Z} := \sum_{l=1}^{L} \mathbf{Z}_l \colon \mathbb{R}^d \times [t_n, t_n + k] \to \mathbb{R}^m
$$

be the solution of the initial value problem

$$
\partial_t \mathbf{Z}_l + \nabla \cdot (\mathbf{Z}_l\tilde{\underline{a}}_l) = \mathbf{0} \tag{38}
$$

$$
\mathbf{Z}_l(t_n) = \mathbf{S}_l(\mathbf{U}(t_n)) + \frac{k}{2}\mathbf{T}_l(\mathbf{U}(t_n), \nabla\mathbf{U}(t_n)). \tag{39}
$$

Then

$$\mathbf{Z}(t_n + k) - \mathbf{U}(t_n + k) = \mathcal{O}(k^3). \tag{40}$$

Proof. As before, we expand $\mathbf{Z}(t)$ in a Taylor series. At time $t = t_n$, we obtain

$$\mathbf{Z}_t = -\nabla \cdot \sum \mathbf{Z}_l \underline{\tilde{a}}_l$$
$$\mathbf{Z}_{tt} = -\nabla \cdot \sum (\mathbf{Z}_l)_t \underline{\tilde{a}}_l,$$

and therefore

$$\begin{aligned}
\mathbf{Z} - \mathbf{V} &= -\sum \left(\mathbf{S}_l(\mathbf{U}) + \frac{k}{2} \mathbf{T}_l(\mathbf{U}, \nabla \mathbf{U}) \right) - \mathbf{U} = \mathbf{0} \\
\mathbf{Z}_t - \mathbf{V}_t &= -\nabla \cdot \sum \left(\mathbf{S}_l(\mathbf{U}) + \frac{k}{2} \mathbf{T}_l(\mathbf{U}, \nabla \mathbf{U}) - \mathbf{S}_l(\mathbf{U}) \right) \underline{\tilde{a}}_l \\
&= -\frac{k}{2} \nabla \cdot \sum \mathbf{T}_l(\mathbf{U}, \nabla \mathbf{U}) \underline{\tilde{a}}_l \\
\mathbf{Z}_{tt} - \mathbf{V}_{tt} &= -\nabla \cdot \sum ((\mathbf{Z}_l)_t - \mathbf{S}_l'(\mathbf{V}) \mathbf{V}_t) \underline{\tilde{a}}_l \\
&= \nabla \cdot \sum \left(\nabla \cdot (\mathbf{Z}_l \underline{\tilde{a}}_l) - \mathbf{S}_l'(\mathbf{V}) \nabla \cdot \sum \mathbf{S}_k(\mathbf{V}) \underline{\tilde{a}}_k \right) \underline{\tilde{a}}_l \\
&= \nabla \cdot \sum (\nabla \cdot (\mathbf{S}_l(\mathbf{U}) \underline{a}_l(\mathbf{U})) - \mathbf{S}_l'(\mathbf{U}) \nabla \cdot \underline{\mathbf{F}}(\mathbf{U})) \underline{\tilde{a}}_l + \mathcal{O}(k) \\
&= \nabla \cdot \sum \mathbf{T}_l(\mathbf{U}, \nabla \mathbf{U}) \underline{\tilde{a}}_l + \mathcal{O}(k).
\end{aligned}$$

This implies that

$$(\mathbf{Z} - \mathbf{V})(t_n + k) = \mathcal{O}(k^3),$$

and (40) now follows from (32). ■

Let us mention once more that for the Euler equations and the shallow-water equations, Morel, Fey, and Maurer have also derived a second-order-accurate decomposition into linear advection equations. However, since they freeze the advection velocities at the beginning of the timestep, their linearization is only first-order accurate in time. As a consequence, they have to add correction terms for a mixed linearization and decomposition error, which results in a solution that is computationally more expensive than ours. Note that, recently, Zimmermann [48] has derived a different decomposition for the Euler equations which is related to second-order kinetic schemes and evaluates the velocities at the half-timestep as well.

3. SOLVING THE ADVECTION EQUATIONS BY CHARACTERISTIC SCHEMES

The linearization and decomposition given in the previous section leads us, at the beginning of each timestep, to a set of scalar transport equations of the form

$$\partial_t \varphi + \nabla \cdot (\varphi \underline{a}) = 0. \tag{41}$$

In this section, we discuss several ways to discretize (41). In Section 3.2, we show that a notorious inconsistency at sonic points, which is well known for several finite-volume schemes, appears also for a standard first-order discretization of (41). In Section 3.3, we modify this discretization and prove first- and second-order consistency of our new method.

For the rest of this section, we assume that the velocity field $\underline{a}\colon \mathbb{R}^d \times \mathbb{R}_+ \to \mathbb{R}^d$ is a given *smooth* function of $\underline{x}$ and t. In Section 4 we will indicate how to treat *piecewise smooth* velocity fields, which arise from the discretization of the full system of conservation laws (1).

The scalar function $\varphi\colon \mathbb{R}^d \times \mathbb{R}_+ \to \mathbb{R}$ is the unknown, and initial data are prescribed at $t = t_n := nk$,

$$\varphi(x, t_n) = \varphi_D(x). \tag{42}$$

Equations (41), (42) may be solved by introducing the characteristics $\underline{\xi}(\tau; \underline{x}, t)$ by

$$\begin{aligned} \underline{\xi}&\colon \mathbb{R}_+ \times \mathbb{R}^d \times \mathbb{R}_+ \to \mathbb{R}^d \\ \underline{\xi}(t; \underline{x}, t) &= \underline{x} \\ \partial_\tau \underline{\xi}(\tau; \underline{x}, t) &= \underline{a}(\underline{\xi}(\tau; \underline{x}, t), \tau). \end{aligned} \tag{43}$$

Since the flux vector $\varphi\underline{a}$ is always parallel to the characteristics, we have the following:

LEMMA 3.1. *For all* $K \subset \mathbb{R}^d$, $t, \tau \in \mathbb{R}_+$,

$$\frac{d}{d\tau} \int\limits_{\underline{\xi}(\tau; K, t)} \varphi(\underline{x}, \tau)\, d\underline{x} = 0. \tag{44}$$

3.1. Characteristic Schemes

We would like to use Lemma 3.1 to construct numerical methods for solving (41). For simplicity, we restrict the analysis from now on to two spatial dimensions and use the notation $\underline{x} = (x, y) \in \mathbb{R}^2$ for the space variable, $\underline{a} = (a, b) \in \mathbb{R}^2$ for the velocity field, and $\underline{\xi} = (\xi, \eta)$ for the characteristics. In the Remark following Definition 3.2, we will generalise our new scheme to an arbitrary number of space dimensions and indicate the treatment of curvilinear grids.

For $i, j \in \mathbb{Z}$ let $(x_i, y_j) := (ih, jh)$ be the points and let

$$\begin{aligned} K_{ij} &:= \left[x_{i-1/2}, x_{i+1/2}\right] \times \left[y_{j-1/2}, y_{j+1/2}\right] \\ &:= [x_i - h/2, x_i + h/2] \times [y_j - h/2, y_j + h/2] \end{aligned} \tag{45}$$

be the cells of a uniform Cartesian grid with mesh space $h = \Delta x = \Delta y$. Recall that $k = \Delta t$ is the timestep. Lemma 3.1 gives

$$\int\limits_{K_{ij}} \varphi(\underline{x}, t_{n+1})\, d\underline{x} = \sum_{i', j'} \left(\int\limits_{K_{i'j'} \cap \underline{\xi}(t_n; K_{ij}, t_{n+1})} \varphi(\underline{x}, t_n)\, d\underline{x} \right). \tag{46}$$

Note that $K_{i'j'} \cap \underline{\xi}(t_n; K_{ij}, t_{n+1})$ is that part of $K_{i'j'}$ that will be mapped to K_{ij} by the characteristic flow from time t_n to time t_{n+1} (see Fig. 2).

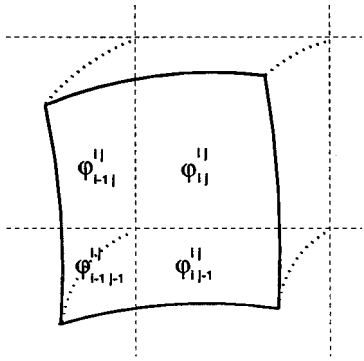

FIG. 2. Backward characteristic transport of cell K_{ij} for the case $a, b > 0$. The region bounded by the curved lines is $\underline{\xi}(t_n; K_{ij}, t_{n+1})$, and the dotted lines are backward characteristic curves issuing from the corners of cell K_{ij}. The dashed lines are the grid lines.

DEFINITION 3.1. Let $\overline{\varphi}_{ij}^n$ be an approximation of the cell average of the solution of the linear advection equation (41) at time t_n,

$$\overline{\varphi}_{ij}^n \approx \frac{1}{|K_{ij}|} \int_{K_{ij}} \varphi(\underline{x}, t_n)\, d\underline{x} \tag{47}$$

and let the *wave* $\overline{\varphi}_{i'j'}^{ij}$ approximate the flow from cell $K_{i'j'}$ to cell K_{ij} from time t_n to time t_{n+1},

$$\overline{\varphi}_{i'j'}^{ij} \approx \frac{1}{|K_{ij}|} \int_{K_{i'j'} \cap \underline{\xi}(t_n; K_{ij}, t_{n+1})} \varphi(\underline{x}, t_n)\, d\underline{x}. \tag{48}$$

A *characteristic scheme* for (41) is then given by

$$\overline{\varphi}_{ij}^0 := \frac{1}{|K_{ij}|} \int_{K_{ij}} \varphi_D(\underline{x})\, d\underline{x} \tag{49}$$

$$\overline{\varphi}_{ij}^{n+1} := \sum_{i', j'} \overline{\varphi}_{i'j'}^{ij}. \tag{50}$$

We always assume the *conservativity* property

$$\sum_{i', j'} \overline{\varphi}_{ij}^{i'j'} = \overline{\varphi}_{ij}^n, \tag{51}$$

where the waves $\overline{\varphi}_{ij}^{i'j'}$ are defined as in (48).

Remark. (i) Definition 3.1 is essentially due to Fey. Note that the waves $\overline{\varphi}_{i'j'}^{ij}$ and $\overline{\varphi}_{ij}^{i'j'}$ may be interpreted in two ways: Eq. (50) states that the cell average of φ over cell K_{ij} at the new time t_{n+1} is a sum of waves $\overline{\varphi}_{i'j'}^{ij}$ which flow from all neighbors $K_{i'j'}$ (including $(i', j') = (i, j)$) into the cell K_{ij}. The dual interpretation is given by (51): the cell-average of φ over cell K_{ij} at the old time t_n may be decomposed into waves $\overline{\varphi}_{ij}^{i'j'}$ which flow out of the cell to the neighbors $K_{i'j'}$.

(ii) Using (51) the update (50) may be rewritten in the conservative form

$$\overline{\varphi}_{ij}^{n+1} = \overline{\varphi}_{ij}^{n} + \sum_{i',j'} \left(\overline{\varphi}_{i'j'}^{ij} - \overline{\varphi}_{ij}^{i'j'} \right). \tag{52}$$

One may think of the quantity $\overline{\varphi}_{i'j'}^{ij} - \overline{\varphi}_{ij}^{i'j'}$ as an approximation of the integral of the flux between cells $K_{i'j'}$ and K_{ij} over the time interval $[t_n, t_{n+1}]$.

(iii) In the numerical algorithms presented below, the approximation of (48) will come in two steps. The first step will be a spatial reconstruction of $\varphi(\cdot, t_n)$ by piecewise constant or piecewise linear functions φ_R. We will label the corresponding schemes *P0* and *P1* respectively. The second step will be the approximation of the characteristic flow $K_{i'j'} \cap \underline{\xi}(t_n; K_{ij}, t_{n+1})$. This will be done either by cell-centered evolution or by interface-centered evolution, and we will use the acronyms *CCE* and *ICE* to distinguish these two approaches.

For the moment, let us consider schemes using piecewise constant reconstructions and focus on the approximation of the characteristic flow.

NOTATION 3.1. *In the following, we will use notation of the form*

$$a_{i+(1/2)j}^{n} := a\left(x_{i+1/2}, y_j, t_n\right) \tag{53}$$

for a, b, and φ. Whenever no confusion is possible, we will drop the superscript n.

3.2. Cell-Centered Evolution: The *MoT-CCE*

In a series of papers [7–11], Fey and collaborators have used a cell-centered approximation of the characteristic flow. When combined with piecewise constant reconstructions, Fey's scheme is defined as follows:

In each cell K_{ij}, consider the local characteristic flow defined by

$$\begin{aligned} \underline{\xi}_{ij}^{n}(t; \underline{x}, t) &:= \underline{x} \\ \partial_\tau \underline{\xi}_{ij}^{n}(\tau; \underline{x}, t) &:= \underline{a}(x_i, y_j, t_n) = \underline{a}_{ij}^{n}, \end{aligned} \tag{54}$$

so that each local approximation $\underline{\xi}_{ij}^{n}$ of the flow is defined using the constant velocity field $\underline{a}_{ij}^{n} = \underline{a}(x_i, y_j, t_n)$. Then set

$$K_{i'j'}^{ij} := K_{i'j'} \cap \underline{\xi}_{i'j'}^{n}(t_n; K_{ij}, t_{n+1}) \tag{55}$$

and

$$\overline{\varphi}_{i'j'}^{ij} := \frac{1}{|K_{ij}|} \int_{K_{i'j'}^{ij}} \varphi_R(\underline{x})\, d\underline{x} = \frac{\left|K_{i'j'}^{ij}\right|}{|K_{ij}|} \overline{\varphi}_{i'j'}. \tag{56}$$

In one spatial dimension this leads to the algorithm

$$\begin{aligned} \overline{\varphi}_i^{n+1} &:= \overline{\varphi}_{i-1}^{i} + \overline{\varphi}_i^{i} + \overline{\varphi}_{i+1}^{i} \\ &= \lambda(a_{i-1}) + \overline{\varphi}_{i-1} + (1 - \lambda|a_i|)\overline{\varphi}_i - \lambda(a_{i+1})_- \overline{\varphi}_{i+1}, \end{aligned} \tag{57}$$

where $\lambda := k/h$ and the subscripts $\pm$ denote the positive and negative parts of a quantity. Here we have assumed the CFL (Courant–Friedrichs–Lewy) condition

$$\lambda \max_{i,n} \left| a_i^n \right| \leq 1, \tag{58}$$

and so the update in cell K_i is only affected by the values of the old solutions in the neighboring cells.

Fey calls his scheme *MoT* (Method of Transport), and therefore we will use the acronym *MoT-CCE-P0* for his scheme with piecewise constant reconstructions.

Let us discuss the consistency of the *MoT-CCE-P0* with the differential equation (41). If $\underline{a}$ is constant, then (56) coincides with the first-order upwind scheme. For variable coefficients the situation is more complex. Let us consider two examples.

EXAMPLE 3.1. First let us consider the case

$$a(x,t) = -x$$

corresponding to a compressive wave ($\nabla \cdot a < 0$). For constant initial data,

$$\varphi_D(x) \equiv 1,$$

the exact solution remains constant in space but grows exponentially in time,

$$\varphi(x,t) \equiv e^t.$$

The approximate solution produced by the *MoT-CCE-P0* is

$$\overline{\varphi}_i^n = \begin{cases} (1+k)^n, & i \neq 0 \\ 2(1+k)^n - 1, & i = 0. \end{cases}$$

As k tends to zero with λ fixed, this solution converges to

$$\varphi^{\text{approx}}(x,t) := \begin{cases} e^t, & x \neq 0 \\ 2e^t - 1, & x = 0. \end{cases}$$

Thus (56) is inconsistent with the differential equation (41) at the "sonic" point $x = 0$, where the transport velocity a changes sign. The cell-centered evolution leads to an inconsistent approximation of $\nabla \cdot \underline{a}$, which takes the value 2 instead of 1. This situation is illustrated in Fig. 3.

EXAMPLE 3.2. As a complementary example, let us consider the case of a rarefaction wave, $\nabla \cdot \underline{a} > 0$:

$$a(x,t) = x, \quad \varphi_D(x) \equiv 1.$$

In this case the exact solution is

$$\varphi(x,t) \equiv e^{-t}$$

and the approximate solution is

$$\overline{\varphi}_i^n = \begin{cases} (1-k)^n, & i \neq 0 \\ 1, & i = 0. \end{cases}$$

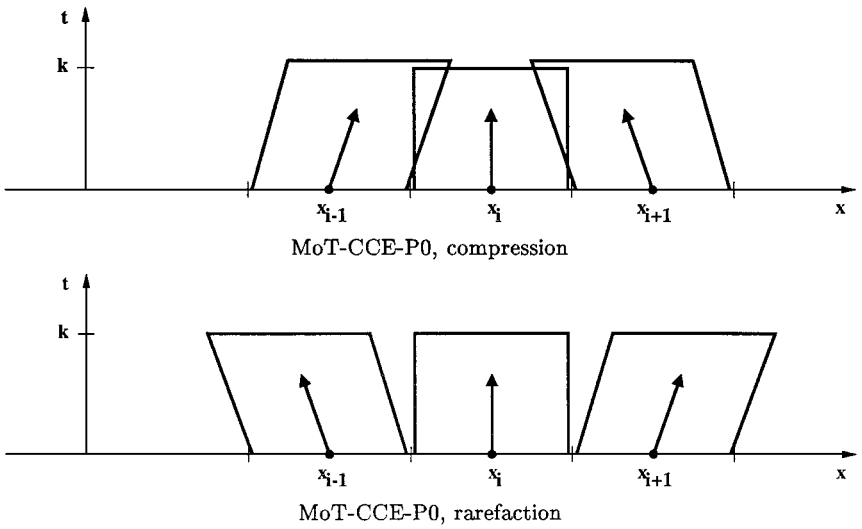

FIG. 3. Approximate characteristic flow for the *MoT-CCE-P0* in one spatial dimension. Compression field (top) and rarefaction field (bottom). Each cell K_i is transported forwards in time using the constant velocity a_i^n. Note the resulting gaps for the rarefaction and the overlaps for the compression.

As k tends to zero with λ fixed, this solution converges to

$$\varphi^{\text{approx}}(x,t) := \begin{cases} e^{-t}, & x \neq 0 \\ 1, & x = 0 \end{cases}$$

so we have an analogous inconsistency.

A similar difficulty was already described by Steger and Warming in 1981 [40]: the numerical flux produced by their splitting is not continuously differentiable at sonic points for the equations of gasdynamics (i.e., points where the magnitude of the fluid velocity $|u|$ equals the sound velocity c, so one eigenvalue of $u \pm c$ vanishes). This results in so-called glitches at the sonic points. Subsequently, Van Leer [43] developed a splitting with continuously differentiable fluxes (compare also the discussion in Chapter 20.2.3 of Hirsh's textbook [15]).

In her dissertation, Morel [26] also observed glitches at sonic points for two-dimensional shallow-water computations carried out with the *MoT-CCE-P0*, and she generalized the Van Leer flux-vector-splitting to two dimensions to remove these numerical artifacts. However, this slows down the algorithm considerably, and Morel herself remarks that her method does not seem to be generalizable to second-order accuracy. Compare our numerical experiments in Section 5.5 below.

Let us also remark that in Examples 3.1 and 3.2 above, the *MoT-CCE-P0* diverges in the L^∞-norm but converges in L^1. Moreover, this inconsistency does not occur when one approximates the velocity field $\underline{a}$ by piecewise linear functions; i.e., Fey's *MoT-CCE-P*1 may very well be second-order consistent, even at sonic points.

For similar difficulties at sonic points in the context of upwind finite-difference schemes we refer the reader to [38].

3.3. Interface-Centered Evolution: The *MoT-ICE*

For the rest of this section, we will derive an alternative to the cell-centered evolution discussed above and prove its consistency. Since the new scheme will approximate the characteristic flow by an extrapolation of the transport velocities which is centered at the *interfaces* between the cells, we will call it *MoT-ICE* for interface-centered evolution.

As we have seen at the beginning of this section, it is crucial to approximate the characteristic flow $\underline{\xi}(\cdot; \underline{x}, t_n)$ along the velocity field $\underline{a}$ from time t_n to time t_{n+1}, or equivalently, the backwards characteristic flow $\underline{\xi}(\cdot; \underline{x}, t_{n+1})$ from time t_{n+1} to time t_n. Let $L^{x,n}_{j+1/2}$ be the curve in the (x, y)-plane that will be mapped to the horizontal grid line $\mathbb{R} \times \{y_{j+1/2}\}$ by the forward flow. Using the notation $\underline{\xi} = (\xi, \eta)$ for the characteristics we may write

$$L^{x,n}_{j+1/2} := \left\{\underline{x} \mid \eta(t_{n+1}; \underline{x}, t_n) = y_{j+1/2}\right\} = \underline{\xi}\left(t_n; \mathbb{R} \times \left\{y_{j+1/2}\right\}, t_{n+1}\right). \tag{59}$$

Similarly, let $L^{y,n}_{i+1/2}$ be the curve which will be mapped to the vertical grid line $\{x_{i+1/2}\} \times \mathbb{R}$,

$$L^{y,n}_{i+1/2} := \left\{\underline{x} \mid \xi(t_{n+1}; \underline{x}, t_n) = x_{i+1/2}\right\} = \underline{\xi}\left(t_n; \left\{x_{i+1/2}\right\} \times \mathbb{R}, t_{n+1}\right). \tag{60}$$

For small values of $k = \Delta t$ and smooth velocity fields $\underline{a}$, the curve $L^{x,n}_{j+1/2}$ is almost horizontal, and the curve $L^{y,n}_{i+1/2}$ is almost vertical. See the upper two plots of Fig. 4.

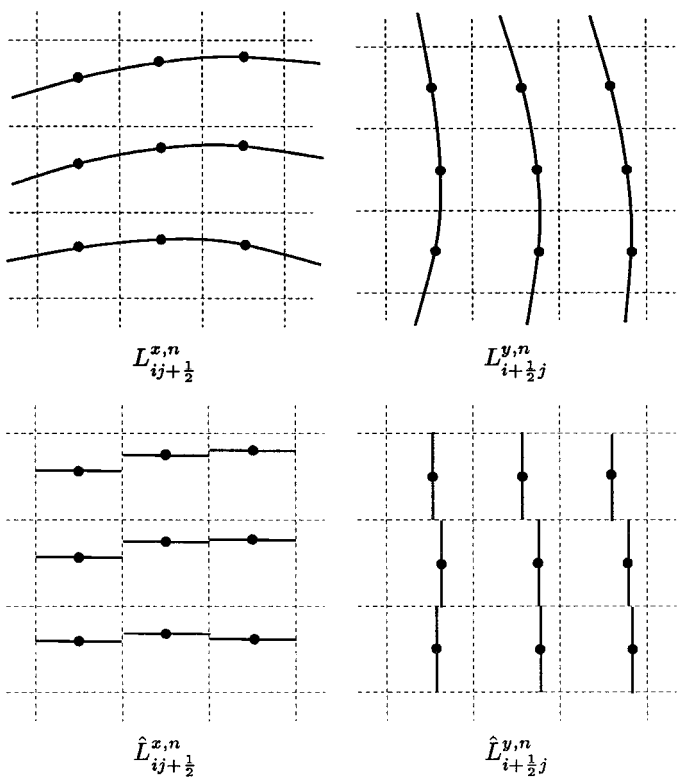

FIG. 4. Backward characteristic transport of the grid lines from time t_{n+1} to t_n ($a, b > 0$). Upper row: original grid at t_{n+1} (dashed lines) and transformed horizontal and vertical lines at t_n (full lines). Lower row: approximation of the transformed grid at t_n by horizontal and vertical line segments. The dots are the midpoints $\underline{m}^{x,n}_{ij+1/2}$, $\underline{m}^{y,n}_{i+(1/2)j}$, (and an approximation of these).

We rewrite the two curves as the union of small segments of approximate length h,

$$L^{x,n}_{j+1/2} = \bigcup_{i\in\mathbf{Z}} L^{x,n}_{i,j+1/2} \tag{61}$$

with

$$L^{x,n}_{ij+1/2} := \left\{ \underline{x} \in L^{x,n}_{j+1/2} \,\middle|\, x \in \left[x_{i-1/2}, x_{i+1/2}\right] \right\} \tag{62}$$

and

$$L^{y,n}_{i+1/2} = \bigcup_{j\in\mathbf{Z}} L^{y,n}_{i+(1/2)j} \tag{63}$$

with

$$L^{y,n}_{i+(1/2)j} := \left\{ \underline{x} \in L^{y,n}_{i+1/2} \,\middle|\, y \in \left[y_{j-1/2}, y_{j+1/2}\right] \right\}. \tag{64}$$

We will approximate the curved segment $L^{x,n}_{ij+1/2}$ by a horizontal line segment

$$\hat{L}^{x,n}_{ij+1/2} := \left[x_{i-1/2}, x_{i+1/2}\right] \times \left\{\hat{y}_{ij+1/2}\right\}. \tag{65}$$

and approximate the segment $L^{y,n}_{i+(1/2)j}$ by a vertical line segment

$$\hat{L}^{y,n}_{i+(1/2),j} := \left\{\hat{x}_{i+(1/2)j}\right\} \times \left[y_{j-1/2}, y_{j+1/2}\right]. \tag{66}$$

This is illustrated in the lower two plots of Fig. 4.

Let us summarize this: first we have traced the gridlines backwards along the characteristic flow, leading to almost horizontal curves $L^{x,n}_{j+1/2}$ and almost vertical curves $L^{y,n}_{i+1/2}$. Then we have approximated these curves by unions of horizontal line segments and unions of vertical line segments respectively.

Note that so far, the definition of the line segments is incomplete, since we have not yet defined the values $\hat{x}_{i+(1/2)_j}$ and $\hat{y}_{ij+1/2}$.

Let

$$\underline{m}^{x,n}_{ij+1/2} = \left(x_i, y^*_{ij+1/2}\right) \in L^{x,n}_{ij+1/2} \tag{67}$$

$$\underline{m}^{y,n}_{i+(1/2)j} = \left(x^*_{i+(1/2)j}, y_j\right) \in L^{y,n}_{i+(1/2)j}. \tag{68}$$

be the midpoints of the segments $L^{x,n}_{ij+1/2}$ and $L^{y,n}_{i+(1/2)j}$ respectively. Then the midpoints $(x_i, \hat{y}_{ij+1/2})$ of $\hat{L}^{x,n}_{ij+1/2}$ and $(\hat{x}_{i+(1/2)j}, y_i)$ of $\hat{L}^{y,n}_{i+(1/2)j}$ should satisfy

$$\hat{x}_{i+(1/2)j} = x^*_{i+(1/2)j} + \mathcal{O}(h^{p+1}) \tag{69}$$

$$\hat{y}_{ij+1/2} = y^*_{ij+1/2} + \mathcal{O}(h^{p+1}), \tag{70}$$

respectively.

We will see later on that for $p = 1$ and $p = 2$, this is sufficient for pth-order accuracy (see Theorems 3.1 and 3.2 below).

Let us approximate $x^*_{i+(1/2)j}$: From the definition of the characteristic flow (43), any point $\underline{x}$ satisfies

$$\underline{\xi}(t_{n+1};\underline{x},t_n)-\underline{x}=\int_{t_n}^{t_{n+1}}\partial_\tau\underline{\xi}(\tau;\underline{x},t_n)\,d\tau=\int_{t_n}^{t_{n+1}}\underline{a}(\underline{\xi}(\tau;\underline{x},t_n),\tau)\,d\tau. \tag{71}$$

We now choose $\underline{x}=\underline{m}^{y,n}_{i+(1/2)j}$ and take the x-component of (71). From the definition (60) of the segment $L^{y,n}_{i+(1/2)j}$ we obtain

$$x_{i+1/2}-x^*_{i+(1/2)j}=\int_{t_n}^{t_{n+1}}a\big(\underline{\xi}\big(\tau;m^{y,n}_{i+(1/2)j},t_n\big),\tau\big)\,d\tau. \tag{72}$$

Now we will approximate the time integral by a quadrature rule,

$$\frac{1}{k}\int_{t_n}^{t_{n+1}}a\big(\underline{\xi}\big(\tau;\underline{m}^{y,n}_{i+(1/2)j},t_n\big),\tau\big)\,d\tau=\hat{a}^n_{i+(1/2)j}+\mathcal{O}(k^p). \tag{73}$$

So $\hat{a}^n_{i+(1/2)j}$ is an approximation of the mean value of the x-component a of the velocity field $\underline{a}$ along the characteristic $\underline{\xi}$ issuing from the midpoint $\underline{m}^{y,n}_{i+(1/2)j}$ of the segment $L^{y,n}_{i+(1/2)j}$ at time t_n and arriving at the line $\{x_{i+1/2}\}\times\mathbb{R}$ at time t_{n+1}.

Using the explicit Euler timestep to approximate the integral we obtain

$$\frac{1}{k}\int_{t_n}^{t_{n+1}}a\big(\underline{\xi}\big(\tau;\underline{m}^{y,n}_{i+(1/2)j},t_n\big),\tau\big)\,d\tau=a\big(\underline{m}^{y,n}_{i+(1/2)j},t_n\big)+\mathcal{O}(k)=a^n_{i+(1/2)j}+\mathcal{O}(k), \tag{74}$$

where we have used (72) and the fact that for uniformly bounded velocity fields $\underline{a}$,

$$\underline{m}^{y,n}_{i+(1/2)j}=\big(x^*_{i+(1/2)j},y_j\big)=\big(x_{i+1/2},y_j\big)+\mathcal{O}(k). \tag{75}$$

Next let us approximate (73) to second order. From (72) and (74) we have

$$x^*_{i+(1/2)j}=x_{i+1/2}-ka^n_{i+(1/2)j}+\mathcal{O}(k^2). \tag{76}$$

Together with the mid point rule in time and a Taylor expansion of $a(\underline{\xi}(t_{n+1/2};(x,y_j),t_n)$ around $x=x_{i+1/2}-ka^n_{i+(1/2)j}$ this gives

$$\begin{aligned}&\frac{1}{k}\int_{t_n}^{t_{n+1}}a\big(\underline{\xi}\big(\tau;\underline{m}^{y,n}_{i+(1/2)j},t_n\big),\tau\big)\,d\tau\\&=a\big(\underline{\xi}\big(t_{n+1/2};\underline{m}^{y,n}_{i+(1/2)j},t_n\big),t_{n+1/2}\big)+\mathcal{O}(k^2).\\&=a\big(\underline{\xi}\big(t_{n+1/2};\big(x_{i+1/2}-ka^n_{i+(1/2)j},y_j\big),t_n\big),t_{n+1/2}\big)+\mathcal{O}(k^2).\end{aligned} \tag{77}$$

Now we approximate the characteristic transport $\underline{\xi}$ at time $t_{n+1/2}$:

$$\begin{aligned}
&\underline{\xi}\left(t_{n+1/2\,j};\,\left(x_{i+1/2}-ka^n_{i+(1/2)\,j},\,y_j\right),\,t_n\right)\\
&\quad=\left(x_{i+1/2}-ka^n_{i+(1/2)\,j},\,y_j\right)+\frac{k}{2}\left(a^n_{i+(1/2)\,j},\,b^n_{i+(1/2)\,j}\right)+\mathcal{O}(k^2)\\
&\quad=\left(x_{i+1/2}-\frac{k}{2}a^n_{i+(1/2)\,j},\,y_j+\frac{k}{2}b^n_{i+(1/2)\,j}\right)+\mathcal{O}(k^2).
\end{aligned}\tag{78}$$

We use (78) in (77) and Taylor expansions as above to obtain

$$\begin{aligned}
&\frac{1}{k}\int_{t_n}^{t_{n+1}} a\left(\underline{\xi}\left(\tau;\,m^{y,n}_{i+(1/2)\,j},\,t_n\right),\,\tau\right)d\tau\\
&\quad=a\left(x_{i+1/2}-\frac{k}{2}a^n_{i+(1/2)\,j},\,y_j+\frac{k}{2}b^n_{i+(1/2)\,j},\,t_{n+1/2}\right)+\mathcal{O}(k^2)\\
&\quad=\left[a-\frac{k}{2}aa_x+\frac{k}{2}ba_y\right]^{n+1/2}_{i+(1/2)\,j}+\mathcal{O}(k^2).
\end{aligned}\tag{79}$$

Here we have applied Notation 3.1 to the term in square brackets. The value $y^*_{ij+1/2}$ which defines the midpoint $\underline{m}^{x,n}_{ij+1/2}=(x_i,y^*_{ij+1/2})$ of the horizontal line segment $L^{x,n}_{ij+1/2}$ is approximated analogously. These calculations lead us to the folowing definition:

DEFINITION 3.2. The midpoints $\hat{\underline{m}}^{x,n}_{ij+1/2}=(x_i,\hat{y}_{ij+1/2})$ and $\hat{\underline{m}}^{y,n}_{i+(1/2)\,j}=(\hat{x}_{i+(1/2)\,j},y_j)$ of the horizontal and vertical line segments $\hat{L}^{x,n}_{ij+1/2}$ and $\hat{L}^{y,n}_{i+(1/2)\,j}$ respectively are given by

$$\hat{x}_{i+(1/2)\,j}:=x_{i+1/2}-k\hat{a}^n_{i+(1/2)\,j}\tag{80}$$

$$\hat{y}_{ij+1/2}:=y_{j+1/2}-k\hat{b}^n_{ij+1/2}.\tag{81}$$

We define the auxiliary transport velocities $\hat{a}^n_{i+(1/2)\,j}$ and $\hat{b}^n_{ij+1/2}$ by

$$\hat{a}^n_{i+(1/2)\,j}:=a^n_{i+(1/2)\,j}\tag{82}$$

$$\hat{b}^n_{ij+1/2}:=b^n_{ij+1/2},\tag{83}$$

for the *MoT-ICE-P0* and by

$$\hat{a}^n_{i+(1/2)\,j}:=\left[a-\frac{k}{2}aa_x+\frac{k}{2}ba_y\right]^{n+1/2}_{i+(1/2)\,j}\tag{84}$$

$$\hat{b}^n_{ij+1/2}:=\left[b-\frac{k}{2}ab_x-\frac{k}{2}bb_y\right]^{n+1/2}_{ij+1/2}\tag{85}$$

for the *MoT-ICE-P1*.

Remark. The formulae given in Definition 3.2 can be carried over to any number of space dimensions and grids of arbitrary orientation: Let L be a curve segment which is

associated to a cell interface $I \in \mathbb{R}^d$, and let $\underline{x}$ be the midpoint and $\underline{n}$ the normal of I. Then we may approximate the midpoint $\underline{m}$ of L by

$$\frac{1}{k}\int_{t_n}^{t_{n+1}} \underline{a}(\underline{\xi}(\tau;\underline{m},t_n),\tau)\,d\tau = \underline{a}\left(\underline{x} - k(\underline{a}\cdot\underline{n})\underline{n} + \frac{k}{2}\underline{a}\right)\left(\underline{x}, t_{n+1/2}\right) + \mathcal{O}(k^2) \tag{86}$$

and introduce the auxiliary transport velocity $\hat{\underline{a}}$ by

$$\hat{\underline{a}} := \left[\underline{a} - k(\underline{a}\cdot\underline{n})(\underline{n}\cdot\nabla)\underline{a} + \frac{k}{2}(\underline{a}\cdot\nabla)\underline{a}\right]\left(\underline{x}, t_{n+1/2}\right). \tag{87}$$

The midpoint $\hat{\underline{m}}$ of the approximate line segment $\hat{L}$ is then given by

$$\hat{\underline{m}} := \underline{x} - k(\hat{\underline{a}}\cdot\underline{n})\underline{n}. \tag{88}$$

In particular, in the three-dimensional case the *MoT-ICE-P1* has the same simplicity as in the two-dimensional case. Moreover, formulae (87) and (88) may be applied to curvilinear Cartesian grids, as well.

To illustrate the idea of the *MoT-ICE* even more clearly, we display the approximation of the characteristic flow in Fig. 5. We show the same situation as we have done in Fig. 3 for the *MoT-ICE-P0*. For the *MoT-CCE*, *cells* are transported *forwards* in time using an approximation of the characteristic flow at the *cell centers*. For the *MoT-ICE*, *interfaces* between the cells are tracked *backwards* in time using auxiliary transport velocities which are defined at these *interfaces*.

From now on, we let $\lambda = k/h$ and suppose that the CFL condition

$$\lambda \max_{i,j,n}\left\{\left|\hat{a}^n_{i+1/2,j}\right|, \left|\hat{b}^n_{i,j+1/2}\right|\right\} \le 1 \tag{89}$$

is satisfied.

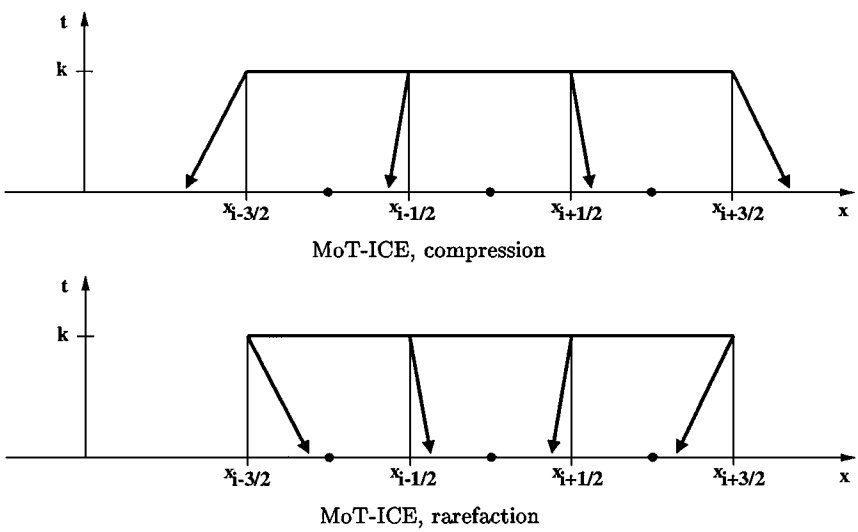

FIG. 5. Approximate characteristic flow for the *MoT-ICE* in one spatial dimension. Compression field (top) and rarefaction field (bottom) (same situation as in Fig. 3). Each cell interface $I_{i+1/2}$ is tracked backwards in time using the auxiliary transport velocity $\hat{a}^n_{i+1/2}$.

Let us look once more at Definition 3.1 of the characteristic schemes: to finish the discretization of (41), it remains to define the waves $\overline{\varphi}_{ij}^{i'j'}$ in (50)–(51). We do this as follows: write

$$\overline{\varphi}_{ij}^{i'j'} := \frac{1}{|K_{ij}|} \int\limits_{K_{ij}^{i'j'}} \varphi_R(x,y)\,dx\,dy, \tag{90}$$

where

$$K_{ij}^{i'j'} := \left[x_{ij,L}^{i'}, x_{ij,R}^{i'}\right] \times \left[y_{ij,L}^{j'}, y_{ij,R}^{j'}\right] \tag{91}$$

is that approximation of

$$K_{ij} \cap \underline{\xi}(t_n; K_{i'j'}, t_{n+1})$$

which is constructed by replacing the curved line segments $L_{ij\pm1/2}^{x,n}$ and $L_{i\pm(1/2)j}^{y,n}$ defined in (61)–(64) by the straight line segments $\hat{L}_{ij\pm1/2}^{x,n}$ and $\hat{L}_{i\pm(1/2)j}^{y,n}$ defined in (65) and (66). Using (80) and (81) we obtain

$$x_{ij,L}^{i'} = \begin{cases} x_{i-1/2} & \text{for } i' = i-1 \\ x_{i-1/2} - k\left(\hat{a}_{i-(1/2)j}^n\right)_- & \text{for } i' = i \\ x_{i+1/2} - k\left(\hat{a}_{i+(1/2)j}^n\right)_+ & \text{for } i' = i+1 \end{cases} \tag{92}$$

$$x_{ij,R}^{i'} = \begin{cases} x_{ij,L}^{i'+1} & \text{for } i' \in \{i-1, i\} \\ x_{i+1/2} & \text{for } i' = i+1 \end{cases} \tag{93}$$

$$y_{ij,L}^{j'} = \begin{cases} y_{j-1/2} & \text{for } j' = j-1 \\ y_{j-1/2} - k\left(\hat{b}_{ij-1/2}^n\right)_- & \text{for } j' = j \\ y_{j+1/2} - k\left(\hat{b}_{ij+1/2}^n\right)_+ & \text{for } j' = j+1 \end{cases} \tag{94}$$

$$y_{ij,R}^{j'} = \begin{cases} y_{ij,L}^{j'+1} & \text{for } j' \in \{j-1, j\} \\ y_{j+1/2} & \text{for } j' = j+1 \end{cases} \tag{95}$$

(compare Fig. 6 for the case $\hat{a}, \hat{b} > 0$). Note that for piecewise-constant reconstructions (90) simply becomes

$$\overline{\varphi}_{ij}^{i'j'} := \frac{1}{|K_{ij}|}\left(x_{ij,R}^{i'} - x_{ij,L}^{i'}\right)\left(y_{ij,R}^{j'} - y_{ij,L}^{j'}\right)\overline{\varphi}_{ij} \tag{96}$$

and for piecewise-linear reconstructions $\varphi_R^{ij}(x,y)$ (see (128)),

$$\overline{\varphi}_{ij}^{i'j'} := \frac{1}{|K_{ij}|}\left(x_{ij,R}^{i'} - x_{ij,L}^{i'}\right)\left(y_{ij,R}^{j'} - y_{ij,L}^{j'}\right) \cdot \varphi_R^{ij}\left(\frac{x_{ij,L}^{i'} + x_{ij,R}^{i'}}{2}, \frac{y_{ij,L}^{j'} - y_{ij,R}^{j'}}{2}\right). \tag{97}$$

Remark. Formula (97) should be compared to the *MoT-CCE-P1* in [9]: given a piecewise-linear reconstruction of the velocity fields, the *MoT-CCE-P1* extrapolates the characteristic flow over each cell forwards in time. The cell is thus transformed into a general

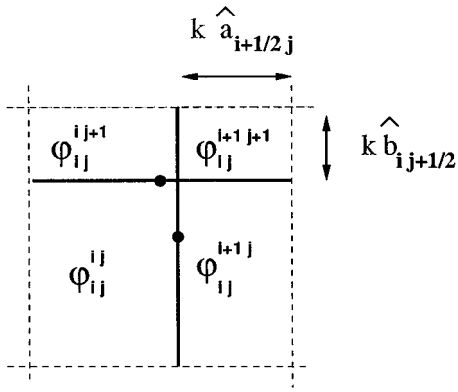

FIG. 6. Auxiliary transport velocities and approximate characteristic decomposition of a two-dimensional cell K_{ij} via interface-centered evolution. This figure is the result of superimposing the lower two plots of Fig. 4 and cutting out cell K_{ij}.

quadrilateral, which has to be projected back onto the grid. Then a piecewise-linear reconstruction of the solution is integrated over each resulting subcell. The necessary quadratures are far more complex than (97). This seems to be the main reason for the gain of efficiency of the *MoT-ICE-P1* (see Section 5.6). We expect an even bigger gain in efficiency for the three-dimensional case.

3.3.1. *Consistency of the MoT-ICE-P0*

In this section, we state and prove first-order consistency of the *MoT-ICE* for piecewise-constant spatial reconstructions of φ. For technical reasons, we will need the following definition:

DEFINITION 3.3. A function f defined at the cell centers is called *discretely Lipschitz continuous* if for neighboring cells K_{ij} and $K_{i'j'}$,

$$f_{ij} - f_{i'j'} = \mathcal{O}(h). \tag{98}$$

Analogously, a function g which is defined at the interfaces between the cells is called discretely Lipschitz continuous if its values at neighboring interfaces differ by no more than $\mathcal{O}(h)$.

THEOREM 3.1. *Suppose that $\lambda = k/h$ is fixed and that the CFL condition* (89) *is satisfied. Suppose that $\tilde{a}_{i+(1/2)j}$ and $\tilde{b}_{ij+1/2}$ are given discretely Lipschitz continuous grid functions, and let the auxiliary transport velocities $\hat{a}$ and $\hat{b}$ be given by*

$$\hat{a}_{i+(1/2)j} = a\big(x_{i+1/2}, y_j, t_n\big) + h\tilde{a}_{i+(1/2)j} \tag{99}$$

$$\hat{b}_{ij+1/2} = b\big(x_i, y_{j+1/2}, t_n\big) + h\tilde{b}_{ij+1/2}. \tag{100}$$

Let the MoT-ICE-P0 for (41) *be defined by* (47), (48), *where the waves $\bar{\varphi}_{ij}^{i'j'}$ are defined by* (96) *together with* (92)–(95).

Then for any given smooth velocity field $\underline{a}: \mathbf{R}^2 \times \mathbf{R}_+ \to \mathbf{R}^2$, the MoT-ICE-P0 is consistent of order one with the differential equation (41).

Note that we have replaced the definition (82), (83) of the auxiliary transport velocities $\hat{a}^n_{i+(1/2)j}$ and $\hat{b}^n_{ij+1/2}$ by the slightly more general version (99), (100). The higher order terms $\tilde{a}_{i+(1/2)j}$ and $\tilde{b}_{ij+1/2}$ allow for some flexibility in the numerical approximation of the auxiliary transport velocites. For example, one might think of approximating $a^n_{i+(1/2)j} = a(x_{i+1/2}, y_j, t_n)$ by $\frac{1}{2}(a^n_{ij} + a^n_{i+1j})$ or by $a^{n+1/2}_{i+(1/2)j}$. If the velocity field $\underline{a}$ is continuously differentiable, then the resulting terms $\tilde{a}_{i+(1/2)j}$ will be discretely Lipschitz continous.

As is evident from Examples 3.1 and 3.2, the difficulty of the proof lies in controlling the truncation error at the sonic points where the transport velocities a and b change their sign.

Proof of Theorem 3.1. Let φ be a smooth solution of (41) with initial data φ_D given at time $t = t_n$, and let

$$\overline{\varphi}^n_{ij} = \frac{1}{|K_{ij}|} \int\limits_{K_{ij}} \varphi_D(\underline{x})\, d\underline{x}. \tag{101}$$

Let $\overline{\varphi}^{n+1}_{ij}$ be the approximate solution computed with the *MoT-ICE-P0*, i.e., (48), (96), and (99), (100). We would like to show that

$$\overline{\varphi}^{n+1}_{ij} - \frac{1}{|K_{ij}|} \int\limits_{K_{ij}} \varphi(\underline{x}, t_{n+1})\, d\underline{x} = \mathcal{O}(h^2). \tag{102}$$

From (41),

$$\begin{aligned}
&\frac{1}{|K_{ij}|} \int\limits_{K_{ij}} \varphi(\underline{x}, k)\, d\underline{x} \\
&= \frac{1}{|K_{ij}|} \int\limits_{K_{ij}} \varphi_D(\underline{x})\, d\underline{x} - \frac{1}{|K_{ij}|} \int\limits_{t_n}^{t_{n+1}} \int\limits_{y_{j-1/2}}^{y_{j+1/2}} \big(a\varphi\big(x_{i+1/2}, y, t\big) - a\varphi\big(x_{i-1/2}, y, t\big)\big)\, dy\, dt \\
&\quad - \frac{1}{|K_{ij}|} \int\limits_{t_n}^{t_{n+1}} \int\limits_{x_{i-1/2}}^{x_{i+1/2}} \big(b\varphi\big(x, y_{j+1/2}, t\big) - b\varphi\big(x, y_{j-1/2}, t\big)\big)\, dx\, dt \\
&= \overline{\varphi}^n_{ij} - \lambda\big((a\varphi)^n_{i+(1/2)j} - (a\varphi)^n_{i-(1/2)j}\big) - \lambda\big((b\varphi)^n_{ij+1/2} - (b\varphi)^n_{ij-1/2}\big) + \mathcal{O}(k^2).
\end{aligned} \tag{103}$$

We rewrite the characteristic formulation (52) of the scheme in conservative form:

$$\overline{\varphi}^{n+1}_{ij} = \overline{\varphi}^n_{ij} - \lambda\big(f_{i+(1/2)j} - f_{i-(1/2)j}\big) - \lambda\big(g_{ij+1/2} - g_{ij-1/2}\big). \tag{104}$$

Here the numerical flux $f_{i+(1/2)j}$ across $I_{i+(1/2)j}$ is given by

$$\begin{aligned}
\lambda f_{i+(1/2)j} := {} & \big(\overline{\varphi}^{i+1j}_{ij} - \overline{\varphi}^{ij}_{i+1j}\big) + \frac{1}{2}\big(\overline{\varphi}^{i+1j}_{ij+1} - \overline{\varphi}^{ij}_{i+1j+1} + \overline{\varphi}^{i+1j+1}_{ij} - \overline{\varphi}^{ij+1}_{i+1j}\big) \\
& + \frac{1}{2}\big(\overline{\varphi}^{i+1j-1}_{ij} - \overline{\varphi}^{ij-1}_{i+1j} + \overline{\varphi}^{i+1j}_{ij-1} - \overline{\varphi}^{ij}_{i+1j-1}\big),
\end{aligned} \tag{105}$$

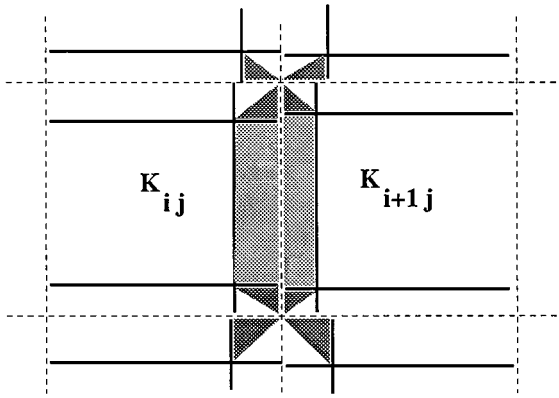

FIG. 7. Contribution to the numerical flux $f_{i+(1/2)j}$ across interface $I_{i+(1/2)j}$ for the *MoT-ICE* in two spatial dimensions. As before, the underlying grid is represented by dashed lines.

and the numerical flux $g_{ij+1/2}$ across $J_{ij+1/2}$ is given analogously by

$$\lambda g_{ij+1/2} := (\bar{\varphi}_{ij}^{ij+1} - \bar{\varphi}_{ij+1}^{ij}) + \frac{1}{2}(\bar{\varphi}_{i-1j}^{ij+1} - \bar{\varphi}_{i-1j+1}^{ij} + \bar{\varphi}_{ij}^{i-1j+1} - \bar{\varphi}_{ij+1}^{i-1j}) + \frac{1}{2}(\bar{\varphi}_{ij}^{i+1j+1} - \bar{\varphi}_{ij+1}^{i+1j} + \bar{\varphi}_{i+1j}^{ij+1} - \bar{\varphi}_{i+1j+1}^{ij}) \tag{106}$$

(see Fig. 7).

To verify (102), it is sufficient to show that

$$f_{i+(1/2)j} - f_{i-(1/2)j} = (a\varphi)_{i+(1/2)j}^{n} - (a\varphi)_{i-(1/2)j}^{n} + \mathcal{O}(h^2) \tag{107}$$

and

$$g_{ij+1/2} - g_{ij-1/2} = (b\varphi)_{ij+1/2}^{n} - (b\varphi)_{ij-1/2}^{n} + \mathcal{O}(h^2) \tag{108}$$

Let us first verify (107). From (104),

$$\begin{aligned}
\lambda f_{i+(1/2)j} \;=\; & (\bar{\varphi}_{ij}^{i+1j+1} + \bar{\varphi}_{ij}^{i+1j} + \bar{\varphi}_{ij}^{i+1j-1}) - (\bar{\varphi}_{i+1j}^{ij+1} + \bar{\varphi}_{i+1j}^{ij} + \bar{\varphi}_{i+1j}^{ij-1}) \\
& + \frac{1}{2}(\bar{\varphi}_{ij+1}^{i+1j} - \bar{\varphi}_{i+1j+1}^{ij} - \bar{\varphi}_{ij}^{i+1j+1} + \bar{\varphi}_{i+1j}^{ij+1}) \\
& - \frac{1}{2}(\bar{\varphi}_{ij}^{i+1j-1} - \bar{\varphi}_{i+1j}^{ij-1} - \bar{\varphi}_{ij-1}^{i+1j} + \bar{\varphi}_{i+1j-1}^{ij}) \\
= \; & \lambda\big[(\hat{a}_{i+(1/2)j})_+ \bar{\varphi}_{ij} + (\hat{a}_{i+(1/2)j})_- \bar{\varphi}_{i+1j}\big] \\
& - \frac{\lambda^2}{2}\big[(\hat{a}_{i+(1/2)j+1})_+ (\hat{b}_{ij+1/2})_- \bar{\varphi}_{ij+1} + (\hat{a}_{i+(1/2)j+1})_- (\hat{b}_{i+1,j+1/2})_- \bar{\varphi}_{i+1,j+1} \\
& + (\hat{a}_{i+(1/2)j})_+ (\hat{b}_{ij+1/2})_+ \bar{\varphi}_{ij} + (\hat{a}_{i+(1/2)j})_- (\hat{b}_{i+1,j+1/2})_+ \bar{\varphi}_{i+1,j}\big] \\
& + \frac{\lambda^2}{2}\big[(\hat{a}_{i+(1/2)j})_+ (\hat{b}_{ij-1/2})_- \bar{\varphi}_{ij} + (\hat{a}_{i+(1/2)j})_- (\hat{b}_{i+1,j-1/2})_- \bar{\varphi}_{i+1,j} \\
& + (\hat{a}_{i+(1/2)j-1})_+ (\hat{b}_{ij-1/2})_+ \bar{\varphi}_{ij-1} + (\hat{a}_{i+(1/2)j-1})_- (\hat{b}_{i+1,j-1/2})_+ \bar{\varphi}_{i+1,j-1}\big] \\
=: \; & \lambda f_{i+(1/2)j}^{C} - \frac{\lambda^2}{2}(f_{i+(1/2)j}^{N} - f_{i+(1/2)j}^{S}).
\end{aligned} \tag{109}$$

This decomposition is shown schematically in Fig. 8.

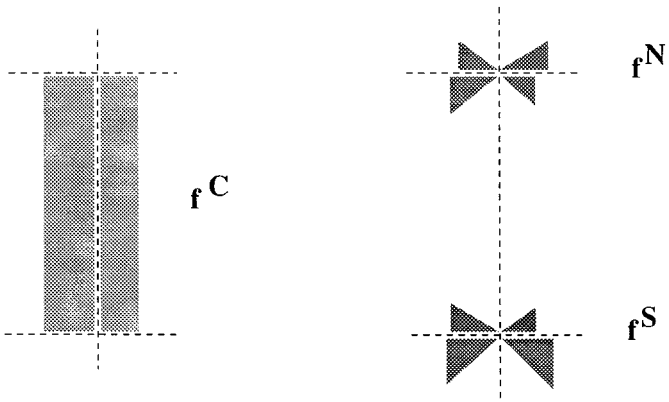

FIG. 8. Decomposition of the numerical flux into central, northern, and southern parts.

The central part of the flux satisfies

$$\begin{aligned} f^{\mathrm{C}}_{i+1/2,\,j} &= \left[\hat{a} + \left(\varphi - \frac{h}{2}\varphi_x\right) - \hat{a} - \left(\varphi + \frac{h}{2}\varphi_x\right)\right]_{i+(1/2)j} + \mathcal{O}(h^2) \\ &= \left(\hat{a}\varphi - \frac{h}{2}|\hat{a}|\varphi_x\right)_{i+(1/2)j} + \mathcal{O}(h^2) \\ &= (a\varphi)_{i+(1/2)j} + h\left(\tilde{a}\varphi - \frac{1}{2}|a|\varphi_x\right)_{i+(1/2)j} + \mathcal{O}(h^2). \end{aligned} \tag{110}$$

Let

$$\alpha := \operatorname{sign} \hat{a}.$$

The contribution from the northern corner satisfies

$$\begin{aligned} f^{\mathrm{N}}_{i+(1/2)j} \;=\; & \left[\hat{a}_+\left(\hat{b} - \frac{h}{2}b_x - \frac{h}{2}b_y\right)_-\left(\varphi - \frac{h}{2}\varphi_x\right)\right. \\ & \left. +\; \hat{a}_-\left(\hat{b} + \frac{h}{2}b_x - \frac{h}{2}b_y\right)_-\left(\varphi + \frac{h}{2}\varphi_x\right)\right]_{i+(1/2)j+1} \\ & + \left[\hat{a}_+\left(\hat{b} - \frac{h}{2}b_x + \frac{h}{2}b_y\right)_+\left(\varphi - \frac{h}{2}\varphi_x\right)\right. \\ & \left. +\; \hat{a}_-\left(\hat{b} + \frac{h}{2}b_x + \frac{h}{2}b_y\right)_+\left(\varphi + \frac{h}{2}\varphi_x\right)\right]_{i+(1/2)j} + \mathcal{O}(h^2) \\ =:\; & f^{\mathrm{N}}_1 + f^{\mathrm{N}}_1 + \mathcal{O}(h^2). \end{aligned} \tag{111}$$

We claim that

$$f^{\mathrm{N}}_1 = \left[\hat{a}\left(\hat{b} - \frac{h}{2}\alpha b_x - \frac{h}{2}b_y\right)_-\left(\varphi - \frac{h}{2}\alpha\varphi_x\right)\right]_{i+(1/2)j+1} + \mathcal{O}(h^2) \tag{112}$$

and

$$f_2^{\mathrm{N}} = \left[\hat{a}\left(\hat{b} - \frac{h}{2}\alpha b_x + \frac{h}{2}b_y\right) + \left(\varphi - \frac{h}{2}\alpha\varphi_x\right)\right]_{i+(1/2)j} + \mathcal{O}(h^2). \tag{113}$$

First we prove (112). Note that the mapping $b \mapsto b_-$ is Lipschitz continuous, and so

$$\left(\hat{b} - \frac{h}{2}b_x - \frac{h}{2}b_y\right)_- = \hat{b}_- + \mathcal{O}(h). \tag{114}$$

Using this and the identities

$$\hat{a}_+ = \frac{\hat{a} + \alpha\hat{a}}{2}, \quad \hat{a}_- = \frac{\hat{a} - \alpha\hat{a}}{2} \tag{115}$$

we obtain

$$\begin{aligned} f_1^{\mathrm{N}} &= \left\{\hat{a}\left[\frac{1+\alpha}{2}\left(\hat{b} - \frac{h}{2}b_x - \frac{h}{2}b_y\right)_- + \frac{1-\alpha}{2}\left(\hat{b} + \frac{h}{2}b_x - \frac{h}{2}b_y\right)_-\right]\varphi \right. \\ &\quad \left. - \frac{h}{2}\hat{a}\hat{b}_-(\alpha\varphi_x)\right\}_{i+(1/2)j+1} + \mathcal{O}(h^2) \\ &= \left[\hat{a}\left(\hat{b} - \frac{h}{2}\alpha b_x - \frac{h}{2}b_y\right)_-\varphi - \frac{h}{2}\hat{a}\hat{b}_-(\alpha\varphi_x)\right]_{i+(1/2)j+1} + \mathcal{O}(h^2) \\ &= \left[\hat{a}\left(\hat{b} - \frac{h}{2}\alpha b_x - \frac{h}{2}b_y\right)_-\left(\varphi - \frac{h}{2}\alpha\varphi_x\right)\right]_{i+(1/2)j+1} + \mathcal{O}(h^2), \end{aligned} \tag{116}$$

i.e., (112). We verify (113) analogously, and in the same way, we obtain

$$f^{\mathrm{S}} = f_1^{\mathrm{S}} + f_2^{\mathrm{S}} + \mathcal{O}(h^2) \tag{117}$$

with

$$f_1^{\mathrm{S}} = \left[\hat{a}\left(\hat{b} - \frac{h}{2}\alpha b_x - \frac{h}{2}b_y\right)_-\left(\varphi - \frac{h}{2}\alpha\varphi_x\right)\right]_{i+(1/2)j} + \mathcal{O}(h^2) \tag{118}$$

and

$$f_2^{\mathrm{S}} = \left[\hat{a}\left(\hat{b} - \frac{h}{2}\alpha b_x + \frac{h}{2}b_y\right)_+\left(\varphi - \frac{h}{2}\alpha\varphi_x\right)\right]_{i+(1/2)j-1} + \mathcal{O}(h^2). \tag{119}$$

Subtracting f^{S} from f^{N}, we obtain

$$\begin{aligned} f_{i+(1/2)j}^{\mathrm{N}} - f_{i+(1/2)j}^{\mathrm{S}} &= h\frac{\partial}{\partial y}\left[\hat{a}\left(\hat{b} - \frac{h}{2}\alpha b_x - \frac{h}{2}b_y\right)_-\left(\varphi - \frac{h}{2}\alpha\varphi_x\right)\right]_{i+(1/2)j+1/2} \\ &\quad + h\frac{\partial}{\partial y}\left[\hat{a}\left(\hat{b} - \frac{h}{2}\alpha b_x + \frac{h}{2}b_y\right)_+\left(\varphi - \frac{h}{2}\alpha\varphi_x\right)\right]_{i+(1/2)j-1/2} + \mathcal{O}(h^2) \\ &= h\frac{\partial}{\partial y}\left[(ab - \varphi)_{i+(1/2)j+1/2} + (ab + \varphi)_{i+(1/2)j-1/2}\right] + \mathcal{O}(h^2) \\ &= h\frac{\partial}{\partial y}(ab\varphi)_{i+(1/2)j} + \mathcal{O}(h^2). \end{aligned} \tag{120}$$

Combining (109), (110), and (120), we obtain

$$f_{i+(1/2)j} = (a\varphi + hr)^n_{i+(1/2)j} + \mathcal{O}(h^2). \tag{121}$$

with

$$r^n_{i+(1/2)j} := \left[\tilde{a}\varphi - \frac{1}{2}|a|\varphi_x - \frac{\lambda}{2}(ab\varphi)_y\right]^n_{i+(1/2)j}. \tag{122}$$

To verify (107) it remains to check that

$$h\left(r^n_{i+(1/2)j} - r^n_{i-(1/2)j}\right) = \mathcal{O}(h^2). \tag{123}$$

This is true because we are assuming that φ, a, and b are smooth and that $\tilde{a}$ is discretely Lipschitz continuous, and so r is discretely Lipschitz continuous. Equality (108) is proved analogously. ■

To get further insight into the failure of consistency of the *MoT-CCE*, we carry out the above analysis for the *MoT-CCE* in one dimension. An elementary calculation leads to

$$f^{\mathrm{CCE}}_{i+1/2} = (a\varphi + hr^{\mathrm{CCE}})^n_{i+1/2} + \mathcal{O}(h^2) \tag{124}$$

with

$$r^{\mathrm{CCE}}_{i+1/2} := \left[-\frac{1}{2}(|a|\varphi)_x\right]_{i+1/2}. \tag{125}$$

The crucial difference between (122) and (125) is that the remainder now contains a *derivative* of $|a|$. At sonic points, a changes its sign, and so $|a|_x$ is *discontinuous*. Therefore, the remainder $r^{\mathrm{CCE}}_{i+1/2}$ fails to be discretely Lipschitz continuous at sonic points, which leads to the inconsistency shown in Examples 3.1 and 3.2.

3.3.2. *Consistency of the MoT-ICE-P1*

Here we state and prove second-order consistency in space and time of the *MoT-ICE* for piecewise-linear spatial reconstructions of φ.

THEOREM 3.2. *Let $\underline{a}: \mathbf{R}^2 \times \mathbf{R}_+ \to \mathbf{R}^2$ be a given smooth velocity field and let $\varphi: \mathbf{R}^2 \times \mathbf{R}_+ \to \mathbf{R}$ be a smooth solution of* (41).

Let $\tilde{a}$ and $\tilde{b}$ be given discretely Lipschitz-continuous grid functions and define the auxiliary transport velocities $\hat{a}$ and $\hat{b}$ by

$$\tilde{a}_{i+(1/2)j} = \left[a - \frac{k}{2}aa_x + \frac{k}{2}ba_y + k^2\tilde{a}\right]^{n+1/2}_{i+(1/2)j} \tag{126}$$

$$\tilde{b}_{ij+1/2} = \left[b + \frac{k}{2}ab_x - \frac{k}{2}bb_y + k^2\tilde{b}\right]^{n+1/2}_{ij+1/2}. \tag{127}$$

Let the MoT-ICE-P1 for (41) *be defined by* (47), (48), *where the waves $\bar{\varphi}^{i'j'}_{ij}$ are defined by* (97) *together with* (92)–(95) *and the piecewise-linear reconstruction φ_R of φ over K_{ij}*

is given by

$$\varphi_R^{ij}(x, y) := \bar{\varphi}_{ij} + (x - x_i)(\overline{\varphi_x})_{ij} + (y - y_j)(\overline{\varphi_y})_{ij}. \tag{128}$$

Here we assume that the discrete derivatives $(\overline{\varphi_x})_{ij}$ *and* $(\overline{\varphi_y})_{ij}$ *may be written in the form*

$$(\overline{\varphi_x})_{ij} = (\varphi_x)_{ij} + h(\tilde{\varphi}_x)_{ij} \tag{129}$$

$$(\overline{\varphi_y})_{ij} = (\varphi_y)_{ij} + h(\tilde{\varphi}_y)_{ij}, \tag{130}$$

for some discretely Lipschitz-continuous grid functions $\widetilde{\varphi_x}$ *and* $\widetilde{\varphi_y}$. *Let* $\lambda = k/h$ *be fixed and suppose that the CFL condition* (89) *holds.*

Then the MoT-ICE-P1 is consistent of order 2 with the differential equation (41).

As in the first-order case, the Lipschitz-continuous higher order terms in (126), (127) permit some flexibility in the numerical implementation of the auxiliary transport velocities, for example the approximation of the derivatives $\underline{a}_x, \underline{a}_y, \underline{a}_t$, etc. (see the proof of Theorem 4.2 for systems of conservation laws.) Similarly, note that the piecewise-linear numerical reconstructions of a smooth function φ based on cell averages $\bar{\varphi}_{ij}$ do not evaluate the derivatives of the function exactly. The auxiliary values $\widetilde{\varphi_x}$ and $\widetilde{\varphi_y}$ take these deviations into account.

In our test calculations in Section 5 we approximate the derivatives $(\overline{\varphi_x})_{ij}$ and $(\overline{\varphi_y})_{ij}$ by a central version of the WENO (Weighted Essentially Non-Oscillatory) reconstruction [16, 23],

$$(\overline{\varphi_x})_{ij} := \frac{1}{h}\,\mathrm{WENO}\,(\bar{\varphi}_{ij} - \bar{\varphi}_{i-1j}, \bar{\varphi}_{i+1j} - \bar{\varphi}_{ij}) \tag{131}$$

$$(\overline{\varphi_y})_{ij} := \frac{1}{h}\,\mathrm{WENO}\,(\bar{\varphi}_{ij} - \bar{\varphi}_{ij-1}, \bar{\varphi}_{ij+1} - \bar{\varphi}_{ij}) \tag{132}$$

with

$$\mathrm{WENO}\,(d_1, d_2) := (\omega_1 d_1 + \omega_2 d_2)/(\omega_1 + \omega_2) \tag{133}$$

and

$$\omega_i := \left(\varepsilon + d_i^2\right)^{-2}. \tag{134}$$

As in [16], we use $\varepsilon := 10^{-6}$. Using similar techniques as in [16], one can verify that the central WENO reconstruction satisfies (129), (130) at all points, including extrema of the solution.

The proof of Theorem 3.2 follows along the lines of that of Theorem 3.1 but requires a much more careful analysis of truncation errors owing to the piecewise-linear reconstruction. Let us stress once more that we do obtain second-order consistency at all points, including those where the transport velocities change sign.

Proof of Theorem 3.2. Let φ be a smooth solution of (41). We want to show that

$$\bar{\varphi}_{ij}^{n+1} - \frac{1}{|K_{ij}|}\int_{K_{ij}} \varphi(\underline{x}, k)\, d\underline{x} = \mathcal{O}(h^3). \tag{135}$$

From (41),

$$\frac{1}{|K_{ij}|}\int_{K_{ij}} \varphi(\underline{x}, t_{n+1})\, d\underline{x} = \overline{\varphi}_{ij}^n - \lambda\left[(a\varphi)_{i+(1/2)j}^{n+1/2} - (a\varphi)_{i-(1/2)j}^{n+1/2}\right] - \lambda\left[(b\varphi)_{ij+1/2}^{n+1/2} - (b\varphi)_{ij-1/2}^{n+1/2}\right] + \mathcal{O}(k^3). \tag{136}$$

Using a Taylor series with a remainder $\tilde{f}$, we obtain

$$\begin{aligned}(a\varphi)_{i+(1/2)j}^{n+1/2} &= \left[a\varphi + \frac{k}{2}(a\varphi)_t + k^2\,\tilde{f}\right]_{i+(1/2)j}^n \\ &= \left[\left(a + \frac{k}{2}a_t\right)\left(1 - \frac{k}{2}(a_x + b_y)\right)\varphi - \frac{k}{2}(a^2\varphi_x + ab\varphi_y) + k^2\psi_a\right]_{i+(1/2)j}^n .\end{aligned} \tag{137}$$

The last equality implicitly defines a discretely Lipschitz continuous function ψ_a. Combining this with (126), we obtain

$$\begin{aligned}(a\varphi)_{i+(1/2)j}^{n+1/2} &= \left[\left(\hat{a} - \frac{k}{2}(ab)_y - k^2\tilde{a}\right)\varphi - \frac{k}{2}(a^2\varphi_x + ab\varphi_y) + k^2\psi_a\right]_{i+(1/2)j}^n \\ &= \left[\hat{a}\varphi - \frac{k}{2}a^2\varphi_x - \frac{k}{2}(ab\varphi)_y - k^2\tilde{a} + k^2\psi_a\right]_{i+(1/2)j}^n \\ &= \left[\hat{a}\left(\varphi - \frac{k}{2}\hat{a}\varphi_x\right) - \frac{k}{2}(\hat{a}\hat{b}\varphi)_y + k^2\psi_a\right]_{i+(1/2)j}^n .\end{aligned} \tag{138}$$

Analogously,

$$(b\varphi)_{ij+1/2}^{n+1/2} = \left[\hat{b}\left(\varphi - \frac{k}{2}\hat{b}\varphi_y\right) - \frac{k}{2}(\hat{a}\hat{b}\varphi)_x + k^2\psi_b\right]_{ij+1/2}^n . \tag{139}$$

Therefore,

$$(a\varphi)_{i+(1/2)j}^{n+1/2} - (a\varphi)_{i-(1/2)j}^{n+1/2} = h\frac{\partial}{\partial x}\left[\hat{a}\left(\varphi - \frac{k}{2}\hat{a}\varphi_x\right) - \frac{k}{2}(\hat{a}\hat{b}\varphi)_y\right]_{ij}^n + \mathcal{O}(h^3) \tag{140}$$

and

$$(a\varphi)_{ij+1/2}^{n+1/2} - (b\varphi)_{ij-1/2}^{n+1/2} = h\frac{\partial}{\partial y}\left[\hat{b}\left(\varphi - \frac{k}{2}\hat{b}\varphi_y\right) - \frac{k}{2}(\hat{a}\hat{b}\varphi)_x\right]_{ij}^n + \mathcal{O}(h^3). \tag{141}$$

As before, we rewrite the update in conservative form (104) and define the numerical fluxes by (104), (105). Plugging (104) and (136)–(141) into (135), we see that it is sufficient

to show

$$f_{i+(1/2)j} - f_{i-(1/2)j} = h\frac{\partial}{\partial y}\left[\hat{a}\left(\varphi - \frac{k}{2}\hat{a}\varphi_x\right) - \frac{k}{2}(\hat{a}\hat{b}\varphi)_y\right]_{ij}^{n} + \mathcal{O}(h^3) \tag{142}$$

and

$$g_{ij+1/2} - g_{ij-1/2} = h\frac{\partial}{\partial y}\left[\hat{b}\left(\varphi - \frac{k}{2}\hat{b}\varphi_y\right) - \frac{k}{2}(\hat{a}\hat{b}\varphi)_x\right]_{ij}^{n} + \mathcal{O}(h^3). \tag{143}$$

First we treat (142). Similarly as in (109), we rewrite the flux as

$$f_{i+(1/2)j} = f^{\mathrm{C}}_{i+(1/2)j} - \frac{\lambda}{2}\left(f^{\mathrm{N}}_{i+(1/2)j} - f^{\mathrm{S}}_{i+(1/2)j}\right) \tag{144}$$

with

$$\begin{aligned} f^{\mathrm{C}}_{i+(1/2)j} := {} & \left(\hat{a}_{i+(1/2)j}\right)_+ \varphi_R^{ij}\left(x_{i+1/2} - \frac{k}{2}\hat{a}_+, y_j\right) \\ & + \left(\hat{a}_{i+(1/2)j}\right)_- \varphi_R^{i+1,j}\left(x_{i+1/2} - \frac{k}{2}\hat{a}_-, y_j\right), \end{aligned} \tag{145}$$

$$\begin{aligned} f^{\mathrm{N}}_{i+(1/2)j} := {} & \left(\hat{a}_{i+(1/2)j+1}\right)_+ \left(\hat{b}_{ij+1/2}\right)_- \varphi_R^{ij+1}\left(x_{i+1/2} - \frac{k}{2}\hat{a}_+, y_{j+1/2} - \frac{k}{2}\hat{b}_-\right) \\ & + \left(\hat{a}_{i+(1/2)j+1}\right)_- \left(\hat{b}_{i+1,j+1/2}\right)_- \varphi_R^{i+1,j+1}\left(x_{i+1/2} - \frac{k}{2}\hat{a}_-, y_{j+1/2} - \frac{k}{2}\hat{b}_-\right) \\ & + \left(\hat{a}_{i+(1/2)j}\right)_+ \left(\hat{b}_{ij+1/2}\right)_+ \varphi_R^{i,j}\left(x_{i+1/2} - \frac{k}{2}\hat{a}_+, y_{j+1/2} - \frac{k}{2}\hat{b}_+\right) \\ & + \left(\hat{a}_{i+(1/2)j}\right)_- \left(\hat{b}_{i+1,j+1/2}\right)_+ \varphi_R^{i+1,j}\left(x_{i+1/2} - \frac{k}{2}\hat{a}_-, y_{j+1/2} - \frac{k}{2}\hat{b}_+\right), \end{aligned} \tag{146}$$

and

$$\begin{aligned} f^{\mathrm{S}}_{i+(1/2)j} := {} & \left(\hat{a}_{i+(1/2)j}\right)_+ \left(\hat{b}_{ij-1/2}\right)_- \varphi_R^{ij}\left(x_{i+1/2} - \frac{k}{2}\hat{a}_+, y_{j-1/2} - \frac{k}{2}\hat{b}_-\right) \\ & + \left(\hat{a}_{i+(1/2)j}\right)_- \left(\hat{b}_{i+1,j-1/2}\right)_- \varphi_R^{i+1,j}\left(x_{i+1/2} - \frac{k}{2}\hat{a}_-, y_{j-1/2} - \frac{k}{2}\hat{b}_-\right) \\ & + \left(\hat{a}_{i+(1/2)j}\right)_+ \left(\hat{b}_{ij-1/2}\right)_+ \varphi_R^{ij-1}\left(x_{i+1/2} - \frac{k}{2}\hat{a}_+, y_{j-1/2} - \frac{k}{2}\hat{b}_+\right) \\ & + \left(\hat{a}_{i+(1/2)j-1}\right)_- \left(\hat{b}_{i+1,j-1/2}\right)_+ \varphi_R^{i+1,j-1}\left(x_{i+1/2} - \frac{k}{2}\hat{a}_-, y_{j-1/2} - \frac{k}{2}\hat{b}_+\right). \end{aligned} \tag{147}$$

Here $\varphi_R^{i,j}$ is defined by (128), and we have simplified the notation as follows: whenever $\hat{a}_\pm$ (respectively $\hat{b}_\pm$) appears twice on the same line, it is evaluated at the same point, and the subscript is dropped at the second occurence.

First we consider the central contributions to the flux, $f^{\mathrm{C}}_{i\pm(1/2)j}$. For $i' \in \{i, i+1\}$, let

$$\psi^{i'j}_{i+(1/2)j}(\tilde{x}) := \frac{1}{h^2}\left[\varphi_R^{i'j}\left(x_{i+1/2} - h\tilde{x}, y_j\right) - (\varphi - h\tilde{x}\varphi_x)_{i+(1/2)j}\right]. \tag{148}$$

Now

$$\begin{aligned} f^{\mathrm{C}}_{i+(1/2)j} &= \left\{\hat{a}_+\left[\left(\varphi - \frac{k}{2}\hat{a}_+\varphi_x\right) + h^2\psi^{ij}\left(\frac{\lambda}{2}\hat{a}_+\right)\right]\right. \\ &\quad \left. + \hat{a}_-\left[\left(\varphi - \frac{k}{2}\hat{a}_-\varphi_x\right) + h^2\psi^{i+1,j}\left(\frac{\lambda}{2}\hat{a}_-\right)\right]\right\}_{i+(1/2)j} \\ &= \left[\hat{a}\left(\varphi - \frac{k}{2}\hat{a}\varphi_x\right)\right]_{i+(1/2)j} + h^2\left[\hat{a}_+\psi^{ij}\left(\frac{\lambda}{2}\hat{a}_+\right) + \hat{a}_-\psi^{i+1,j}\left(\frac{\lambda}{2}\hat{a}_-\right)\right]_{i+(1/2)j} \\ &=: f^{\mathrm{C1}}_{i+(1/2)j} + h^2 f^{\mathrm{C2}}_{i+(1/2)j}. \end{aligned} \tag{149}$$

From this, we obtain

$$f^{\mathrm{C1}}_{i+(1/2)j} - f^{\mathrm{C1}}_{i-(1/2)j} = h\frac{\partial}{\partial x}\left[\hat{a}\left(\varphi - \frac{k}{2}\hat{a}\varphi_x\right)\right]_{ij} + \mathcal{O}(h^3). \tag{150}$$

A straightforward computation using (128), (129), (130), the relation

$$\bar{\varphi}_{ij} = \varphi_{ij} + \frac{h^2}{24}(\varphi_{xx})_{ij} + \mathcal{O}(h^4), \tag{151}$$

and the fact that products and sums of discretely Lipschitz-continuous functions are themselves discretely Lipschitz continuous shows that f^{C2} is discretely Lipschitz continuous, i.e.,

$$h^2\left(f^{\mathrm{C2}}_{i+(1/2)j} - f^{\mathrm{C2}}_{i-(1/2)j}\right) = \mathcal{O}(h^3). \tag{152}$$

Combining (150) and (152) we obtain

$$f^{\mathrm{C}}_{i+(1/2)j} - f^{\mathrm{C}}_{i-(1/2)j} = h\frac{\partial}{\partial x}\left[\hat{a}\left(\varphi - \frac{k}{2}\hat{a}\varphi_x\right)\right]_{ij} + \mathcal{O}(h^3). \tag{153}$$

Next let us consider the contribution to the flux from the upper corner, $f^{\mathrm{N}}_{i+(1/2)j}$. Let $K_{i'j'}$ be any cell which has $(x_{i+1/2}, y_{j+1/2})$ as a corner. Let

$$\begin{aligned} \zeta^{i',j'}_{i+(1/2)j+1/2}(\tilde{x}, \tilde{y}) := \frac{1}{h^2}\left[\varphi_R^{i'j'}\left(x_{i+1/2} - h\tilde{x}, y_{j+1/2} - h\tilde{y}\right)\right. \\ \left. - \left(\varphi - h\tilde{x}\varphi_x - h\tilde{y}\varphi_y\right)_{i+(1/2)j+1/2}\right]. \end{aligned} \tag{154}$$

We can now rewrite f^{N} as

$$\begin{aligned} f^{\mathrm{N}}_{i+(1/2)j} &= (\varphi)_{i+(1/2)j+1/2} f^{\mathrm{N1}}_{i+(1/2)j} - \frac{k}{2}(\varphi_x)_{i+(1/2)j+1/2} f^{\mathrm{N2}}_{i+(1/2)j} \\ &\quad - \frac{k}{2}(\varphi_y)_{i+(1/2)j+1/2} f^{\mathrm{N3}}_{i+(1/2)j} + h^2 f^{\mathrm{N4}}_{i+(1/2)j} \end{aligned} \tag{155}$$

with

$$f^{\mathrm{N1}}_{i+(1/2)j} := (\hat{a}_{i+(1/2)j+1})_+(\hat{b}_{ij+1/2})_- + (\hat{a}_{i+(1/2)j+1})_-(\hat{b}_{i+1,j+1/2})_- + (\hat{a}_{i+(1/2)j})_+(\hat{b}_{ij+1/2})_+ + (\hat{a}_{i+(1/2)j})_-(\hat{b}_{i+1,j+1/2})_+, \tag{156}$$

$$f^{\mathrm{N2}}_{i+(1/2)j} := (\hat{a}_{i+(1/2)j+1})^2_+(\hat{b}_{ij+1/2})_- + (\hat{a}_{i+(1/2)j+1})^2_-(\hat{b}_{i+1,j+1/2})_- + (\hat{a}_{i+(1/2)j})^2_+(\hat{b}_{ij+1/2})_+ + (\hat{a}_{i+(1/2)j})^2_-(\hat{b}_{i+1,j+1/2})_+, \tag{157}$$

$$f^{\mathrm{N3}}_{i+(1/2)j} := (\hat{a}_{i+(1/2)j+1})_+(\hat{b}_{ij+1/2})^2_- + (\hat{a}_{i+(1/2)j+1})_-(\hat{b}_{i+1,j+1/2})^2_- + (\hat{a}_{i+(1/2)j})_+(\hat{b}_{ij+1/2})^2_+ + (\hat{a}_{i+(1/2)j})_-(\hat{b}_{i+1,j+1/2})_+, \tag{158}$$

and

$$\begin{aligned} f^{\mathrm{N4}}_{i+(1/2)j} := {} & (\hat{a}_{i+(1/2)j+1})_+(\hat{b}_{ij+1/2})_- \zeta^{i,j+1}_{i+1/2,j+1/2}\left(\frac{\lambda}{2}\hat{a}_+, \frac{\lambda}{2}\hat{b}_-\right) \\ & + (\hat{a}_{i+(1/2)j+1})_-(\hat{b}_{i+1,j+1/2})_- \zeta^{i+1,j+1}_{i+(1/2)j+1/2}\left(\frac{\lambda}{2}\hat{a}_-, \frac{\lambda}{2}\hat{b}_-\right) \\ & + (\hat{a}_{i+(1/2)j})_+(\hat{b}_{ij+1/2})_+ \zeta^{i,j}_{i+(1/2)j+1/2}\left(\frac{\lambda}{2}\hat{a}_+, \frac{\lambda}{2}\hat{b}_+\right) \\ & + (\hat{a}_{i+(1/2)j})_-(\hat{b}_{i+j,j+1/2})_+ \zeta^{i+1,j}_{i+(1/2)j+1/2}\left(\frac{\lambda}{2}\hat{a}_-, \frac{\lambda}{2}\hat{b}_+\right). \end{aligned} \tag{159}$$

An analogous representation holds for $f^{\mathrm{S}}_{i+(1/2)j}$. Using the same arguments as in the derivation of (152), one shows that

$$h^2\left(f^{\mathrm{N4}}_{i+(1/2)j} - f^{\mathrm{S4}}_{i+(1/2)j}\right) = \mathcal{O}(h^3). \tag{160}$$

The coefficients f^{N2} and f^{N3} consist of smooth terms of $\mathcal{O}(1)$ and $\mathcal{O}(h)$ and of a remainder which is a discretely Lipschitz-continuous function multiplied by h^2. Therefore,

$$\begin{aligned} -\frac{k}{2}\big[& (\varphi_x)_{i+(1/2)j+1/2} f^{\mathrm{N2}}_{i+(1/2)j} - (\varphi_x)_{i+(1/2)j-1/2} f^{\mathrm{S2}}_{i+(1/2)j} \\ & - (\varphi_x)_{i-1/2,j+1/2} f^{\mathrm{N2}}_{i-(1/2)j} + (\varphi_x)_{i-(1/2)j-1/2} f^{\mathrm{S2}}_{i-(1/2)j}\big] = \mathcal{O}(h^3) \end{aligned} \tag{161}$$

and

$$\begin{aligned} -\frac{k}{2}\big[& (\varphi_y)_{i+(1/2)j+1/2} f^{\mathrm{N3}}_{i+(1/2)j} - (\varphi_y)_{i+(1/2)j-1/2} f^{\mathrm{S3}}_{i+(1/2)j} \\ & - (\varphi_y)_{i-(1/2)j+1/2} f^{\mathrm{N3}}_{i-(1/2)j} + (\varphi_y)_{i-(1/2)j-1/2} f^{\mathrm{S3}}_{i-(1/2)j}\big] = \mathcal{O}(h^3). \end{aligned} \tag{162}$$

Finally,

$$\begin{aligned} & \varphi_{i+(1/2)j+1/2} f^{\mathrm{N1}}_{i+(1/2)j} - \varphi_{i+(1/2)j-1/2} f^{\mathrm{S1}}_{i+(1/2)j} - \varphi_{i-(1/2)j+1/2} f^{\mathrm{N1}}_{i-(1/2)j} + \varphi_{i-(1/2)j-1/2} f^{\mathrm{S1}}_{i-(1/2)j} \\ & = h^2\left[\frac{\partial^2}{\partial x\,\partial y}((\hat{a}_+\hat{b}_- + \hat{a}_-\hat{b}_- + \hat{a}_+\hat{b}_+ + \hat{a}_-\hat{b}_+)\varphi)\right]_{ij} + \mathcal{O}(h^3). \\ & = h^2\left[\frac{\partial^2}{\partial x\,\partial y}(ab\varphi)\right]_{ij} + \mathcal{O}(h^3). \end{aligned} \tag{163}$$

Collecting (155)–(163) gives

$$-\frac{\lambda}{2}(f^{\mathrm{N}} - f^{\mathrm{S}})_{i+1/2,j} + \frac{\lambda}{2}(f^{\mathrm{N}} - f^{\mathrm{S}})_{i-1/2,j} = -\frac{kh}{2}(ab\varphi)_{xy} + \mathcal{O}(h^3). \tag{164}$$

Together, (144), (153), and (164) yield (142). Equation (143) is proved analogously. ■

4. THE *MOT-ICE* FOR SYSTEMS OF CONSERVATION LAWS

In this section, we combine the results of Sections 2 and 3 and derive the *MoT-ICE* for systems of conservation laws in two spatial dimensions.

Note that both in Eqs; (126), (127) of Theorem 2.1 and in Eq. (38) of Theorem 3.2 the velocity field $\underline{a} = (a, b)$ is evaluated at the half-timestep $t_{n+1/2}$. In both situations this was done to assure second-order accuracy in time. This simple observation makes it possible to apply the scalar version of the *MoT-ICE-P1* in Theorem 3.2 to the advection equations (38) in Theorem 2.1. To implement it, we need predicted values at the interfaces at the half-timestep $t_{n+1/2}$. These are the values U^* in Algorithms 4.1 and 4.2.

Below we give detailed algorithmic descriptions of the resulting first- and second-order algorithms. We state and prove consistency for smooth solutions and introduce upwind techniques which stabilize discontinuous solutions. Using Eq. (87), it is straightforward to generalize these algorithms to the three-dimensional case.

Let $\underline{x} = (x, y)$ and $\underline{\mathbf{F}} = (\mathbf{F}, \mathbf{G})$ and consider again the system of conservation laws (1), which now reads

$$\partial_t \mathbf{U} + \partial_x \mathbf{F}(\mathbf{U}) + \partial_y \mathbf{G}(\mathbf{U}) = \mathbf{0}. \tag{165}$$

We suppose that a wave model (6), (7) has already been chosen, and we set $\underline{a}_l = (a_l, b_l)$.

Step 0. First define the initial data via

$$\bar{\mathbf{U}}^0_{ij} := \frac{1}{|K_{ij}|} \int_{K_{ij}} \mathbf{U}(x, y, 0)\, dx\, dy. \tag{166}$$

Then make a conservative (i.e., small) guess of the admissible timestep k_{-1}, for example

$$k_{-1} := \frac{h \cdot \mathrm{CFL}}{\max_{ijl}\left(\left|a_l\left(\bar{\mathbf{U}}^0_{ij}\right)\right|, \left|b_l\left(\bar{\mathbf{U}}^0_{ij}\right)\right|\right)}, \tag{167}$$

where CFL is the Courant number. Now suppose that k_{n-1} and $\bar{\mathbf{U}}^n_{ij}$, $i, j \in \mathbb{Z}$, have already been computed. We want to compute k_n and $\bar{\mathbf{U}}^{n+1}_{ij}$, $i, j \in \mathbb{Z}$.

We begin with the *MoT-ICE-P0.*

ALGORITHEM 4.1. *Step 1: For $i, j \in \mathbb{Z}$ and $l = 1, \ldots, L$ compute the auxiliary transport velocities on the interfaces via*

$$\hat{a}^l_{i+(1/2)j} := a_l\left(\mathbf{U}^*_{i+(1/2)j}\right) \tag{168}$$

$$\hat{b}_{ij+1/2} := b_l\left(\mathbf{U}^*_{ij+1/2}\right), \tag{169}$$

where $\mathbf{U}^*_{i+(1/2)j}$ *and* $\mathbf{U}^*_{ij+1/2}$ *are given by a one-dimensional Lax–Friedrichs step*:

$$\mathbf{U}^*_{i+(1/2)j} := \frac{1}{2}(\mathbf{U}_{ij} + \mathbf{U}_{i+1j}) - \frac{\lambda_{n-1}}{2}(\mathbf{F}(\mathbf{U}_{i+1j}) - \mathbf{F}(\mathbf{U}_{ij})) \tag{170}$$

$$\mathbf{U}^*_{ij+1/2} := \frac{1}{2}(\mathbf{U}_{ij} + \mathbf{U}_{ij+1}) - \frac{\lambda_{n-1}}{2}(\mathbf{G}(\mathbf{U}_{ij+1}) - \mathbf{G}(\mathbf{U}_{ij})). \tag{171}$$

Step 2: Compute the new timestep by

$$k_n := \frac{h \cdot \mathrm{CFL}}{\max_{ijl}\left(\left|\hat{a}^l_{i+(1/2)j}\right|, \left|\hat{b}^l_{ij+1/2}\right|\right)} \tag{172}$$

Where $0 < \mathrm{CFL} \leq 1$ *is the Courant number.*

Step 3: Compute the initial data and the update for each wave $l = 1, \ldots, L$ *as follows*: *For* $i, j \in \mathbb{Z}$ *let*

$$\mathbf{Z}^{l,n}_{ij} := \mathbf{S}_l\left(\bar{\mathbf{U}}^n_{ij}\right) \tag{173}$$

and set

$$\bar{\varphi}_{ij} := \mathbf{Z}^{l,n}_{ij}. \tag{174}$$

Use (96) *with timestep* $k = k_n$, $\hat{a}_{i+(1/2)j} = \hat{a}_{i+(1/2)j}$, *and* $\hat{b}_{i+(1/2)j} = \hat{b}^l_{ij+1/2}$ *to compute*

$$\mathbf{Z}^{l,n+1}_{ij} := \sum_{i',j'} \bar{\varphi}^{ij}_{i'j'}. \tag{175}$$

Step 4: For $i, j \in \mathbb{Z}$, *compute the update of the conservative variables*

$$\bar{\mathbf{U}}^{n+1}_{ij} := \sum_{l=1}^{L} \mathbf{Z}^{l,n+1}_{ij}. \tag{176}$$

This completes the definition of the *MoT-ICE-P0*.

Let us now state the consistency of the *MoT-ICE-P0* for smooth solutions. We omit the proof, since it is analogous to that of Theorem 4.2 below.

THEOREM 4.1 *The MoT-ICE-P0 as defined in Algorithm* 4.1 *is consistent of order one with the conservation law* (165) *for smooth solutions.*

Remark. To guarantee first-order consistency, it would have been sufficient to define

$$\hat{a}^l_{i+(1/2)j} := a_l\left(\frac{1}{2}(\mathbf{U}_{ij} + \mathbf{U}_{i+1j})\right)$$

$$\hat{b}^l_{ij+1/2} := b_l\left(\frac{1}{2}(\mathbf{U}_{ij} + \mathbf{U}_{ij+1})\right).$$

However, this central differencing leads to oscillations when one computes discontinuous solutions. The Lax–Friedrichs predictor step (170), (171) stabilizes the solution. See Fig. 9. We stress that there is some freedom in the algorithm at this stage. For example, one might construct the predicted values on the cell interfaces by a Roe decomposition or other upwind technique.

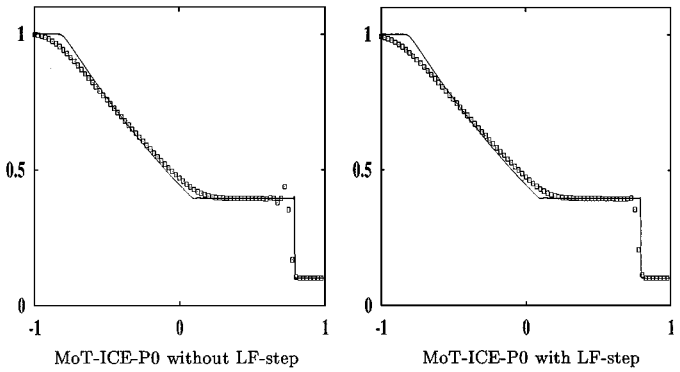

FIG. 9. Density plots for shallow-water Riemann problem (80 points). *MoT-ICE-P0* without and with LF-predictor-step.

For the *MoT-ICE-P1* we need the following modifications:

ALGORITHM 4.2. *Step 1a: For $i, j \in \mathbb{Z}$ and $l = 1, \dots, L$ compute preliminary transport velocities on the interfaces via*

$$a^{l,*}_{i+(1/2)j} := a_l\left(\mathbf{U}^*_{i+(1/2)j}\right) \tag{177}$$

$$b^{l,*}_{i+(1/2)j} := b_l\left(\mathbf{U}^*_{i+(1/2)j}\right) \tag{178}$$

$$a^{l,*}_{ij+1/2} := a_l\left(\mathbf{U}^*_{ij+1/2}\right) \tag{179}$$

$$b^{l,*}_{ij+1/2} := b_l\left(\mathbf{U}^*_{ij+1/2}\right). \tag{180}$$

This time $\mathbf{U}^*_{i+(1/2)j}, \mathbf{U}^*_{ij+1/2}$ are given by the two-dimensional Lax–Friedrichs step

$$\begin{aligned}\mathbf{U}^*_{i+(1/2)j} := {} & \frac{1}{2}(\mathbf{U}_{ij} + \mathbf{U}_{i+1j}) - \frac{\lambda_{n-1}}{2}(\mathbf{F}(\mathbf{U}_{i+1j}) - \mathbf{F}(\mathbf{U}_{ij})) \\ & - \frac{\lambda_{n-1}}{8}(\mathbf{G}(\mathbf{U}_{i+1j+1}) + \mathbf{G}(\mathbf{U}_{ij+1}) - \mathbf{G}(\mathbf{U}_{i+1j-1}) - \mathbf{G}(\mathbf{U}_{ij-1}))\end{aligned} \tag{181}$$

$$\begin{aligned}\mathbf{U}^*_{ij+1/2} := {} & \frac{1}{2}(\mathbf{U}_{ij} + \mathbf{U}_{ij+1}) - \frac{\lambda_{n-1}}{2}(\mathbf{G}(\mathbf{U}_{ij+1}) - \mathbf{G}(\mathbf{U}_{ij})) \\ & - \frac{\lambda_{n-1}}{8}(\mathbf{F}(\mathbf{U}_{i+1j+1}) + \mathbf{F}(\mathbf{U}_{i+1j}) - \mathbf{F}(\mathbf{U}_{i-1j+1}) - \mathbf{F}(\mathbf{U}_{i-1j})).\end{aligned} \tag{182}$$

Step 1b: For $i, j \in \mathbb{Z}$ compute numerical derivatives $(\overline{\mathbf{U}_x})^n_{ij}$ and $(\overline{\mathbf{U}_y})^n_{ij}$ using the central WENO reconstruction (131), (132).

Step 1c: For $i, j \in \mathbb{Z}$ compute numerical derivatives of the transport velocities on the interfaces:

$$(\overline{a_x})^l_{i+(1/2)j} := \frac{1 + \lambda_{n-1}a^{l,*}_{i+(1/2)j}}{2}a'(\overline{\mathbf{U}}_{ij})(\overline{\mathbf{U}_x})_{ij} + \frac{1 - \lambda_{n-1}a^{l,*}_{i+(1/2)j}}{2}a'(\overline{\mathbf{U}}_{i+1j})(\overline{\mathbf{U}_x})_{i+1j} \tag{183}$$

$$(\overline{a_y})^l_{i+(1/2)j} := \frac{1 + \lambda_{n-1}a^{l,*}_{i+(1/2)j}}{2}a'(\overline{\mathbf{U}}_{ij})(\overline{\mathbf{U}_y})_{ij} + \frac{1 - \lambda_{n-1}a^{l,*}_{i+(1/2)j}}{2}a'(\overline{\mathbf{U}}_{i+1j})(\overline{\mathbf{U}_y})_{i+1j} \tag{184}$$

$$(\overline{b_x})^l_{ij+1/2} := \frac{1+\lambda_{n-1}b^{l,*}_{ij+1/2}}{2} b'(\bar{\mathbf{U}}_{ij})(\overline{\mathbf{U}_x})_{ij} + \frac{1-\lambda_{n-1}b^{l,*}_{ij+1/2}}{2} b'(\bar{\mathbf{U}}_{ij+1})(\overline{\mathbf{U}_x})_{ij+1} \tag{185}$$

$$(\overline{b_x})^l_{ij+1/2} := \frac{1+\lambda_{n-1}b^{l,*}_{ij+1/2}}{2} b'(\bar{\mathbf{U}}_{ij})(\overline{\mathbf{U}_y})_{ij} + \frac{1-\lambda_{n-1}b^{l,*}_{ij+1/2}}{2} b'(\bar{\mathbf{U}}_{ij+1})(\overline{\mathbf{U}_y})_{ij+1}. \tag{186}$$

Here $a'(\mathbf{U})$, $b'(\mathbf{U})$ are the gradients of a, b with respect to $\mathbf{U}$.

Step 1d: For $i, j \in \mathbb{Z}$ compute the auxiliary transport velocities:

$$\hat{a}^l_{i+(1/2)j} := \left(a^{l,*}_{i+(1/2)j}\right)\left(1 - \frac{k_{n-1}}{2}(\overline{a_x})^l_{i+(1/2)j}\right) + \frac{k_{n-1}}{2}\left(b^{l,*}_{i+(1/2)j}\right)(\overline{a_y})_{i+(1/2)j} \tag{187}$$

$$\hat{b}^l_{ij+1/2} := \left(b^{l,*}_{ij+1/2}\right)\left(1 - \frac{k_{n-1}}{2}(\overline{b_x})^l_{ij+1/2}\right) + \frac{k_{n-1}}{2}\left(a^{l,*}_{ij+1/2}\right)(\overline{b_x})^l_{ij+1/2}. \tag{188}$$

Step 2: Compute the new timestep k_n by (172).

Step 3: Compute the initial data and the update for each wave $l = 1, \ldots, L$ as follows: *For $i, j \in \mathbb{Z}$ let*

$$\mathbf{Z}^{l,n}_{ij} := \mathbf{S}_l\left(\bar{\mathbf{U}}^n_{ij}\right) + \frac{k_n}{2} T_l\left(\bar{\mathbf{U}}^n_{ij}, (\overline{\mathbf{U}_x})^n_{ij}, (\overline{\mathbf{U}_y})^n_{ij}\right) \tag{189}$$

and set

$$\bar{\varphi}_{ij} := \mathbf{Z}^{l,n}_{ij} \tag{190}$$

$$(\bar{\varphi}_x)_{ij} := \mathbf{S}'_l\left(\bar{\mathbf{U}}^n_{ij}\right)(\overline{\mathbf{U}_x})^n_{ij} \tag{191}$$

$$(\bar{\varphi}_y)_{ij} := \mathbf{S}'_l\left(\bar{\mathbf{U}}^n_{ij}\right)(\overline{\mathbf{U}_y})^n_{ij}. \tag{192}$$

Then use (128) *and* (97) *with timestep $k = k_n$, $\hat{a}_{i+(1/2)j} = \hat{a}^l_{i+(1/2)j}$, and $\hat{b}_{i+(1/2)j} = \hat{b}^l_{ij+1/2}$ to compute*

$$\mathbf{Z}^{l,n+1}_{ij} := \sum_{i',j'} \bar{\varphi}^{ij}_{i'j'}. \tag{193}$$

Step 4: For $i, j \in \mathbb{Z}$ compute the update of the conservative variables by (176).

Remark. (i) In practice, we usually replaced the two-dimensional predictor–steps (181), (182) by the simpler one-dimensional steps (170), (171). This did not have any visible effect on the computed solution.

(ii) The numerical derivatives of the transport velocities on the interfaces defined in (183)–(186) are upwind-weighted averages of the derivatives to the left and right. Without this careful upwinding, the numerical solution may develop instabilities at discontinuities similar to those in Fig. 9.

(iii) In most of our experiments, the scheme was stable for CFI numbers up to unity. There was one exception, namely a radially symmetric implosion for the shallow-water equations. At the moment where the radially symmetric shock focuses at the origin and the

water height develops a sharp peak, one has to reduce the CFL number to 0.5 to maintain stability.

In other cases it seems to be possible to extend the scheme to CFL numbers greater than unity by propagating waves across several cells as in [12, 19].

We end this section by proving the consistency of the *MoT-ICE-P1*.

THEOREM 4.2. *The Mot-ICE-P1 as defined in Algorithm* 4.2 *is consistent of order two with the conservation law* (165) *for smooth solutions.*

Proof. Let us briefly sketch the ingredients of the proof. In Theorem 2.1, we have decomposed the system of conservation laws into the advection equations (38) for the components $\mathbf{Z}_l$ with initial data $\mathbf{Z}_l(t_n)$ given by (39). In (189) of Algorithm 4.2, the initial data for $\mathbf{Z}_l(t_n)$ are approximated to second-order accuracy. The numerical approximation (190)–(193) of $\mathbf{Z}_l(t_{n+1})$ implements the scalar version of the *MoT-ICE-P1* defined in Theorem 3.2. The hypothesis (126), (127) of that theorem can be verified from (177)–(188) by direct computation. It is here that the flexibility which is allowed by the discretely Lipschitz-continuous higher order terms $\tilde{a}$ and $\tilde{b}$ is really needed. We have already remarked that our central WENO reconstruction satisfies (129), (130). Thus we can apply Theorem 3.2 and conclude that $\mathbf{Z}_l(t_{n+1})$ is approximated to second-order accuracy. This concludes the proof. ∎

5. NUMERICAL EXPERIMENTS

In this section we present numerical experiments which confirm the accuracy and stability of the new *MoT-ICE* for smooth and discontinuous solutions. In Section 5.1–5.3 we treat one- and two-dimensional scalar problems with variable coefficients. In Sections 5.4 and 5.5 we compute solutions to the shallow-water equations. We include a preliminary comparison of cpu times in Section 5.6.

5.1. *Scalar Advection with Periodic Coefficients*

To illustrate the failure of consistency of the *MoT-CCE-P0* (cell-centered evolution) and the consistency of the new *MoT-ICE* (interface-centered evolution), we consider the one-dimensional scalar advection equation

$$\partial_t \varphi + \partial_x (\varphi\, a) = 0$$

over the interval $[-1, 1]$ with

$$a(x, t) \equiv -\sin(\pi x)$$

and

$$\varphi_0(x) \equiv 1.$$

Note that at $x = 0$, $\varphi(0, t)$ statistics the ordinary differential equation

$$\partial_t \varphi(0, t) = \pi \varphi(0, t),$$

and so

$$\varphi(0, t) = e^{\pi t}.$$

Similarly,

$$\varphi(1, t) = e^{-\pi t}$$

and these are the maximum and minimum of the exact solution. We compute the solution at time $T = \log(2)/\pi$; so

$$0.5 \leq \varphi(x, T) \leq 2.$$

We choose a CFL number of $4\ \log(2)/\pi$, roughly 0.88. In Table I, we list the experimental orders of convergence (EOCs) with respect to both the L^1 and L^∞ norms.

In the L^1 norm, the EOC of the *MoT-CCE-P0* starts at 0.77 and increases toward 1. However, the method *diverges* in L^∞, as should have been expected from Examples 3.1 and 3.2. In contrast to that, the *MoT-ICE* converges uniformly (i.e., in L^1 and L^∞) to the expected orders. Comparing the L^1 errors of the *MoT-CCE-P0* and the *MoT-ICE-P0* (piecewise-constant reconstructions), one sees that the *MoT-ICE* converges with a better rate (especially on the coarser grids) and produces roughly half the error of the *MoT-CCE*. The convergence rates of the *MoT-ICE-P1* (piecewise-linear reconstructions) are even better than 2 on the finer grids, both for the unlimited and the limited version (we omit the table for the unlimited scheme). The error of the scheme using the WENO limiter is only slightly larger than that of the unlimited scheme and it is of course orders of magnitude smaller than that of the first-order *MoT-ICE-P0*.

TABLE I
EOCs for One-Dimensional Advection with Periodic Coefficients

ix	L_1	EOC	L_∞	EOC
		MoT-CCE-P0		
40	5.456309e-02	—	3.439066e-01	—
80	3.210264e-02	0.77	4.215299e-01	−0.29
160	1.731594e-02	0.89	4.617376e-01	−0.13
320	8.996724e-03	0.94	4.813319e-01	−0.06
640	4.587514e-03	0.97	4.908176e-01	−0.03
		MoT-ICE-P0		
40	3.075886e-02	—	8.834546e-02	—
80	1.599486e-02	0.94	4.741382e-02	0.90
160	8.114853e-03	0.98	2.471667e-02	0.94
320	4.094363e-03	0.99	1.263470e-02	0.97
640	2.055908e-03	0.99	6.379015e-03	0.99
		MoT-ICE-P1 with WENO limiter		
40	2.193228e-03	—	5.123679e-03	—
80	5.330401e-04	2.04	1.532804e-03	1.74
160	1.281400e-04	2.06	3.878244e-04	1.98
320	2.993688e-05	2.10	7.604266e-05	2.35
640	5.934229e-06	2.33	1.523297e-05	2.32

5.2. *Rotating Smooth Hump*

Our next test problem is the two-dimensional scalar equation (41) with

$$a(x, y, t) := -y$$
$$b(x, y, t) := x$$

in the domain $[-1, 1]^2$. Note that for this problem, the *MoT-CCE-P0* and the *MoT-ICE-P0* will produce identical results, since $a_x \equiv b_y \equiv 0$, and so

$$\hat{a}_{i+(1/2)j} = a_{i+(1/2)j} = a_{ij} = -y_j \quad \text{for all } j$$

and

$$\hat{b}_{ij+1/2} = b_{ij+1/2} = b_{ij} = x_i \quad \text{for all } i.$$

We compute one full rotation, i.e., $T = \pi$, and fix $\lambda = \Delta t/\Delta x = \pi/6$. Assuming that the maximal transport velocity is $\sqrt{2}$, this corresponds to a CFL number of roughly 0.74.

First, we consider smooth initial data. Let $x_0 := 0.5$, $y_0 := 0$, $r_0 := 0.3$,

$$r(x, y) := ((x - x_0)^2 + (y - y_0)^2)^{1/2},$$

and

$$\varphi_0(x, y) := \begin{cases} \frac{1}{4}(1 + \cos(\pi r(x, y)/r_0))^2, & \text{if } r < r_0, \\ 0, & \text{otherwise.} \end{cases}$$

For the *MoT-ICE-P0* the EOCs increase slowly toward unity both in L^1 and L^∞ (see Table II). The error is very large on the coarser grids, and the convergence is initially slow.

TABLE II
EOCs for a Smooth Rotating Hump

ix	L_1	EOC	L_∞	EOC	Height
			MoT-ICE-P0		
40	9.528519e-01	—	7.129756e-01	—	0.287
80	6.479957e-01	0.56	5.459218e-01	0.39	0.454
160	3.994583e-01	0.70	3.690224e-01	0.56	0.631
320	2.277596e-01	0.81	2.228099e-01	0.73	0.777
640	1.228174e-01	0.89	1.239005e-01	0.85	0.876
			MoT-ICE-P1 with unlimited central differences		
40	2.596250e-01	—	2.056520e-01	—	0.794
80	5.505040e-02	2.24	4.491245e-02	2.20	0.961
160	1.091899e-02	2.33	8.892373e-03	2.34	0.995
320	2.426323e-03	2.17	1.967944e-03	2.18	0.999
640	5.822946e-04	2.06	4.673955e-04	2.07	1.000
			MoT-ICE-P1 with WENO limiter		
40	4.351708e-01	—	4.749751e-01	—	0.525
80	1.201747e-01	1.86	2.327933e-01	1.03	0.767
160	3.337591e-02	1.85	1.018161e-01	1.19	0.898
320	6.350393e-03	2.39	4.022132e-02	1.34	0.960
640	1.030164e-03	2.62	1.230235e-02	1.71	0.988

TABLE III
EOCs for a Rotating Cylinder

	MoT-ICE-P0			MoT-ICE-P1, WENO limiter		
ix	L_1	EOC	Height	L_1	EOC	Height
40	7.012658e-01	—	0.868	3.758964e-01	—	0.993
80	5.046964e-01	0.47	0.968	2.278516e-01	0.72	1.000
160	3.618134e-01	0.48	0.990	1.398394e-01	0.70	1.000
320	2.583896e-01	0.49	0.995	8.588859e-02	0.70	1.000
640	1.837913e-01	0.49	0.997	5.270885e-02	0.70	1.000

This is natural, since the initial data are not well resolved on the coarse grids, where they appear as a sharp peak rather than a smooth hump.

For the *MoT-ICE-P1* with unlimited central differences the EOCs are better than 2 both in L^1 and L^∞ and they converge toward 2 as the grids are refined. For the *MoT-ICE-P1* with the WENO limiter, the EOCs in L^1 are slightly below 2 in the beginning. However, as the grid is refined, the EOCs increase drastically and well beyond 2. In L^∞, the EOCs start slightly above unity on the underresolved coarse grids, but they show a similar dramatic increase as the grids are refined. In our experience, this behavior is typical for the central WENO limiter.

5.3. *Rotating Cylinder*

Next, we consider the rotating cylinder:

$$\varphi_0(x, y) := \begin{cases} 1 & \text{if } r < r_0, \\ 0 & \text{otherwise.} \end{cases}$$

Since the solution is discontinuous, we only give the experimental orders of convergence in L^1 (see Table III). We also display the maximal height of the cylinder, to see if it is excessively smeared or whether there are overshoots in the numerical solution.

For the *MoT-ICE-P0*, the EOCs tend toward 0.5 as expected for a linear problem and a scheme based on piecewise-constant reconstructions. The maximal height of the cylinder increases toward 1.0 as the grid is refined. For the unlimited *MoT-ICE-P1* (we omit the table), the EOCs are decreasing from 0.78 toward 0.70. As should be expected for a discontinuous solution computed with unlimited piecewise-linear reconstructions, there is an overshoot of 9 to 11% of the height of the cylinder. The *MoT-ICE-P1* with the WENO limiter converges at rate 0.70, produces no overshoots, and yields only slightly larger L^1 errors than the unlimited scheme. As can be seen from the maximal height especially on the coarser grids, the computation is much less smeared than the one with the *MoT-ICE-P0*. The error on the finest grid is a factor 3.5 smaller for the limited *MoT-ICE-P1* than for the *MoT-ICE-P0*. Figure 10 shows that the cylindrical shape of the solution is nicely preserved by both versions of the scheme.

5.4. *Shallow-Water Equations: 1-D Riemann Problem*

In the following two examples, we compute solutions to the shallow-water equations, i.e., Eq. (15) with $\gamma = 2$ and $\kappa = 0.5$. We use the wave model (20)–(22). First we consider

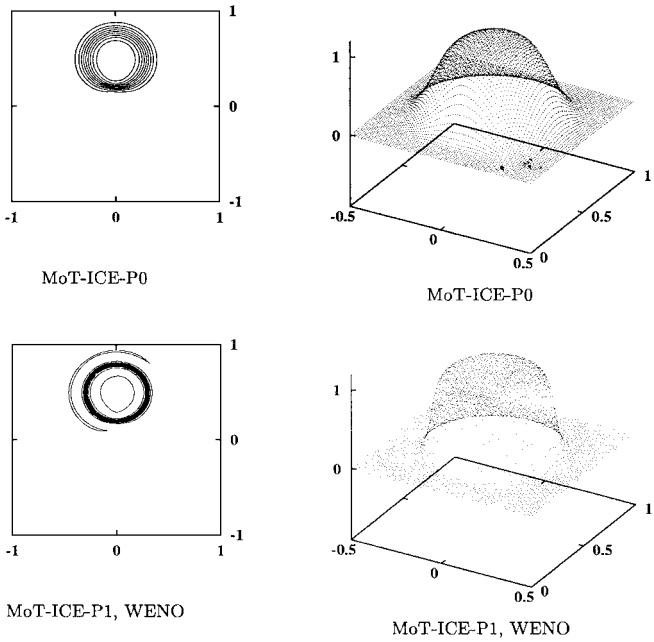

FIG. 10. Rotating cylinder. *MoT-ICE-P0* and *MoT-ICE-P1* (160×160 points).

the one-dimensional Riemann problem with initial data

$$(\rho, u, v) = \begin{cases} (1, 0, 0) & \text{for } x < 0, \\ (0.1, 0, 0) & \text{for } x > 0. \end{cases}$$

We compute the solution at time $T = 0.8$, using a CFI number of 0.8. Note that in this situation, the *MoT-CCE-P0* coincides with the Steger–Warming splitting. As already reported by Steger and Warming in 1981, this scheme produces kinks, or glitches, at sonic points, where the magnitude of the velocity agrees with the sound velocity, $|u| = \sqrt{\rho}$. This can be seen in Fig. 11. The kink near the right corner of the rarefaction wave persists under grid refinement. The numerical solution becomes discontinuous in a region where the exact solution is smooth. The *MoT-ICE*, both with piecewise-constant (*P0*) and piecewise-linear (*P1*) reconstruction produces nonoscillatory results with the expected resolution (see Figs. 12 and 13).

5.5. *Shallow-Water Equations: 2-D Explosion*

In her dissertation [26], Morel computes a radially symmetric explosion for the shallow-water equations with data

$$(\rho, u, v)(x, y, 0) = \begin{cases} (1, 0, 0) & \text{for } (x^2 + y^2)^{1/2} < 0.3 \\ (0.1, 0, 0) & \text{for } (x^2 + y^2)^{1/2} > 0.3. \end{cases}$$

Here we compute this solution over the square $[-1, 1]^2$ with CFL $= 0.8$. Figure 14 shows contour plots of the *MoT-CCE-P0*, the *MoT-ICE-P0*, and the *MoT-ICE-P1* at time $T = 0.6$. It is well known that solutions to radially symmetric problems computed with a first-order Roe or Godunov scheme on a Cartesian grid may become square or diamond shaped

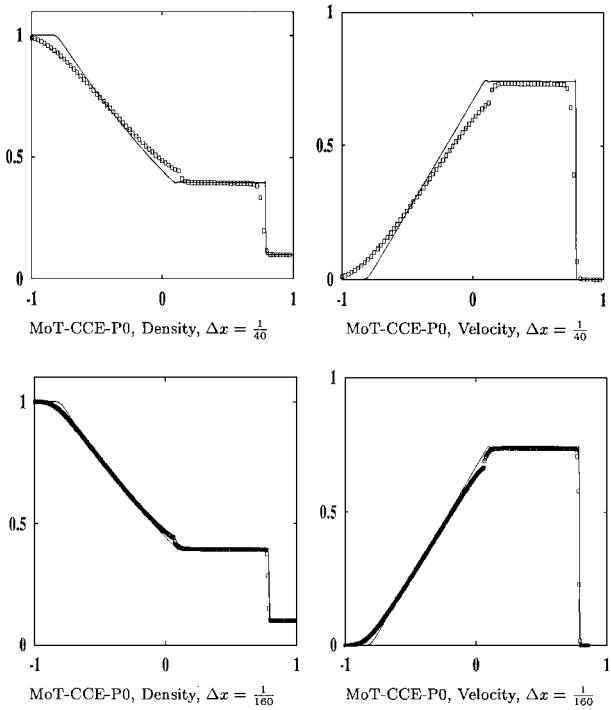

FIG. 11. Shallow-water Riemann problem. *MoT-CCE-P0* with 80 and 320 points. Solid line is the *MoT-ICE-P1* with 800 points. Note the kink of the *MoT-CCE* at the sonic point near the right corner of the rarefaction wave, which persists under grid refinement.

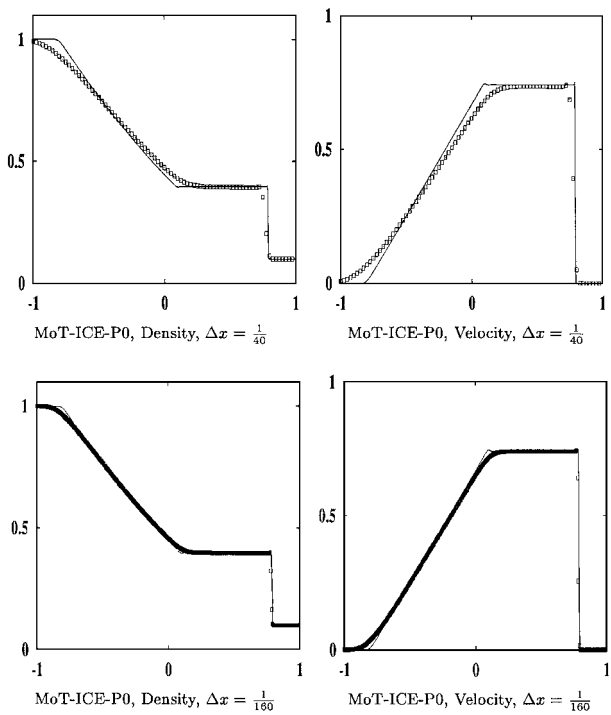

FIG. 12. Same as Fig. 11, but for *MoT-ICE-P0.* There is no kink at the sonic point.

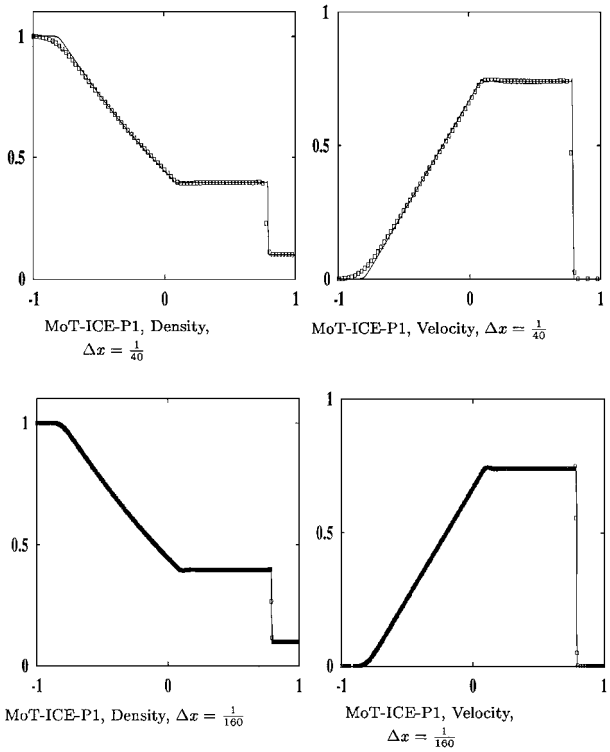

FIG. 13. Same as Fig. 11, but for *MoT-ICE-P1*. There is no kink at the sonic point, and the solution is both accurate and nonoscillatory.

(see for example [22]). The leading shock computed with the *MoT-CCE-P0* is radially symmetric. There are, however, grid-orientation effects at the sonic points in the interior of the solution. The *MoT-ICE*, especially with piecewise-linear reconstruction, produces perfectly radially symmetric results. Details can be seen in Figs. 15–17, where we plot sections along the x-axis and the diagonal against the results of a resolved one-dimensional calculation. The kinks produced by the *MoT-CCE-P0* are clearly visible, but they decrease in magnitude as the grid is refined. Once more, the *MoT-ICE-P0* produces no such kinks. The higher-order-accurate *MoT-ICE-P1* produces a better solution on a grid of 160×160 points than the first-order *MoT-ICE-P0* on a 640×640 grid. On the finest grid, the *MoT-ICE-P1* fully resolves this challenging problem.

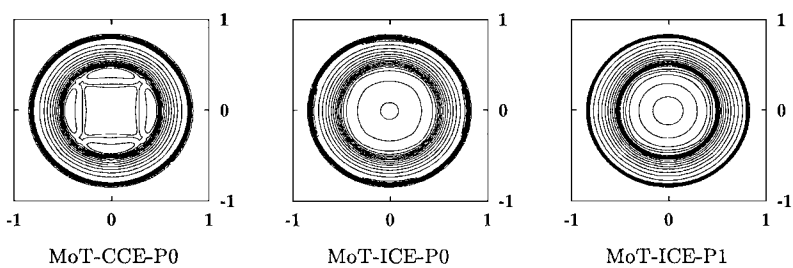

FIG. 14. Explosion prolem for the shallow-water equations using *MoT-CCE-P0*, *MoT-ICE-P0*, and *MoT-ICE-P1* for a grid of 160×160 points with 25 contours of water height.

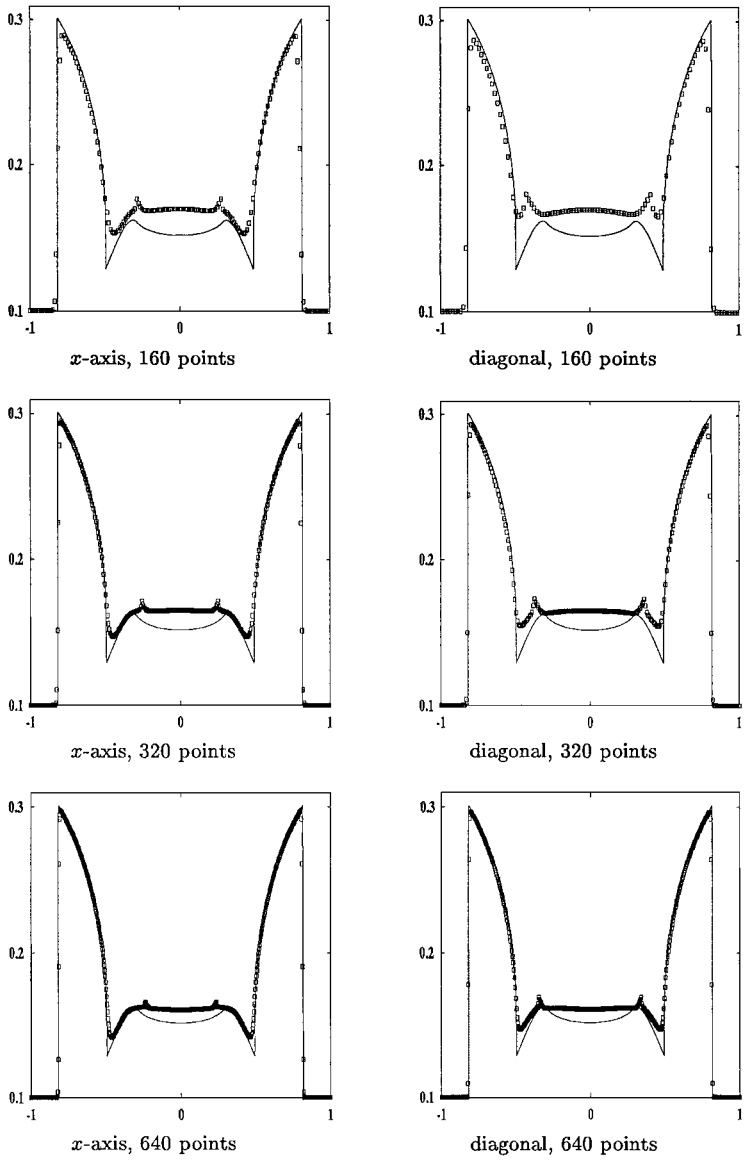

FIG. 15. Explosion problem for the shallow-water equations using *MoT-CCE-P0*. Plots of water height for grids of 160×160, 320×320, and 640×640 points. Left column: cuts along the x-axis. Right column: cuts along the diagonal. Solid line: one-dimensional solution with 3200 points. Note the kinks at the sonic points.

Note that on the fine grid there are two points in the shock region for the *MoT-ICE-P1*, three points for the *MoT-ICE-P0*, and four points for the *MoT-CCE-P0*. From these pictures, the results of the *MoT-ICE-P1* seem to be of the same quality as those computed by Morel [26] using CLAWPACK.

5.6. *Comparison of Efficiencies*

Let us give a first comparison of efficiencies. Morel [26] reports that the *MoT-CCE-P0*, Van Leer's flux-vector splitting, and CLAWPACK $T^{1,0}$ (using the first-order Roe solver

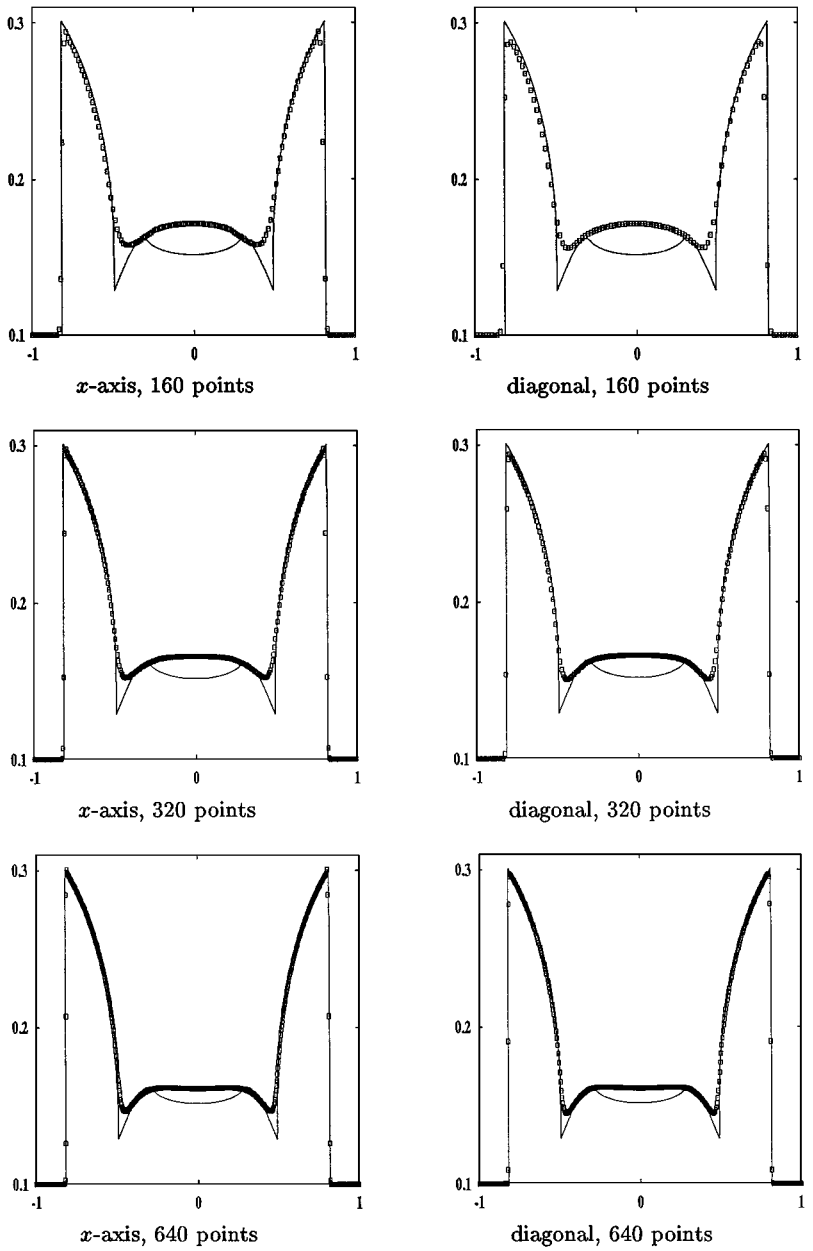

FIG. 16. Same as Fig. 15, but for *MoT-ICE-P0.* Note that the kinks at the sonic points have disappeared.

without transverse wave propagation) all use the same amount of cpu time (say one time unit). CLAWPACK $T^{1,1}$ takes 1.5 units, and the first-order fix at sonic points proposed by Morel takes 2.9 units. Our preliminary experience with the *MoT-ICE* is the following: the *MoT-ICE-P0*, which is consistent at sonic points, takes 0.9 to 1.0 units and is hence as fast as standard first-order schemes. The *MoT-ICE-P1* takes 2.0–2.2 units, which is the same as the second-order CLAWPACK $T^{2,2}$. This compares favorably with the *MoT-CCE-P1* presented in [9], which is consistent at sonic points, but needs 10.5 units of cpu time.

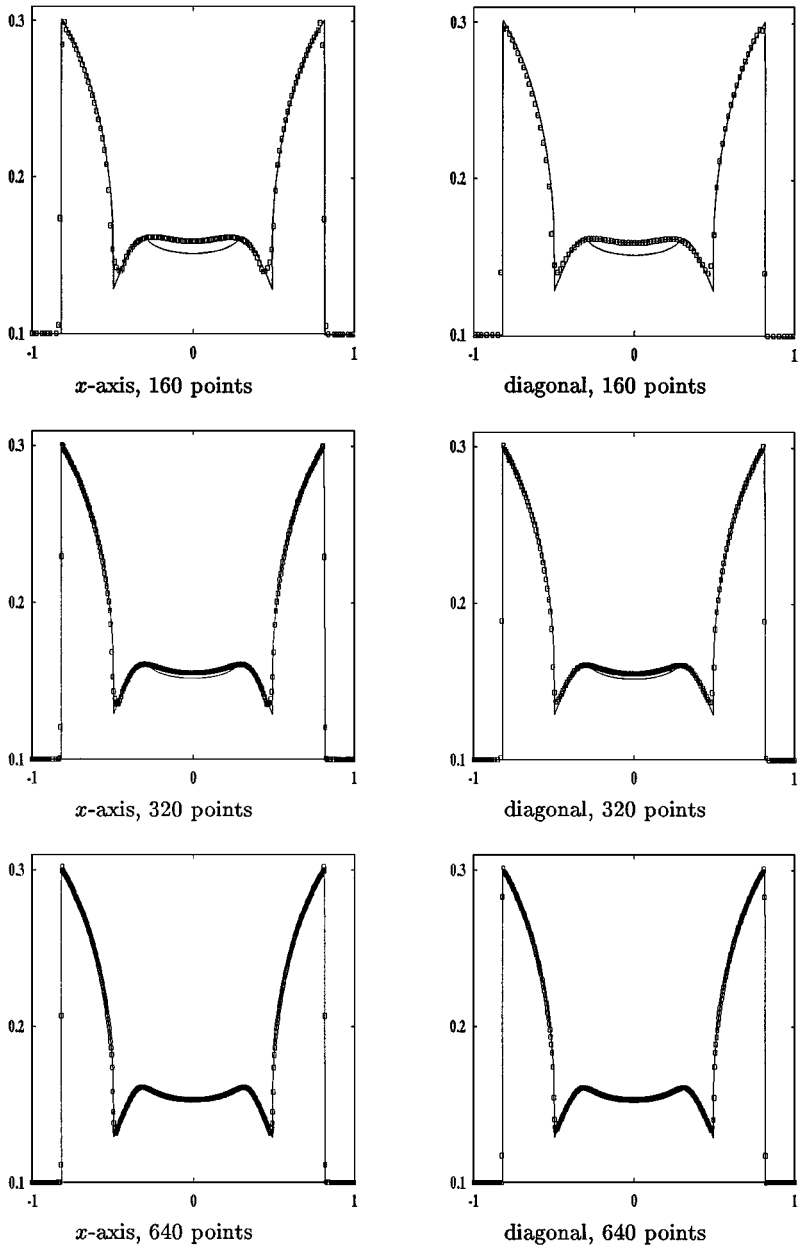

FIG. 17. Same as Fig. 15, but for *MoT-ICE-P1*. There are no kinks, and the resolution is drastically improved.

To fix units, the two-dimensional shallow water explosion described in Section 5.5 above computed with the *MoT-CCE-P0* on a grid of 160×160 points, with Courant number $\mathrm{CFL} = 0.8$ (74 timesteps), took 17.8 seconds of cpu time on a personal computer with 500 MHz Pentium III processor.

6. CONCLUSION

Fey's *multidimensional* Method of Transport is an interesting alternative to schemes based on *one-dimensional* solution operators. Motivated by an inconsistency of the first-order

version of the method at sonic points, which also occurs for other upwind finite-difference schemes, we have developed a uniformly consistent variant of Fey's scheme. Our new scheme is still based on Fey's multidimensional wave models, and on a decomposition of the multidimensional system into scalar advection equations that is similar to his. The key new idea is a different approximation of the characteristic flow at the level of multidimensional scalar advection equations. Fey's method uses a local approximation of the characteristic flow to propagate *cells* forward in time, while our approach tracks the *interfaces* between the cells backward in time. To distinguish between the two approaches, we call Fey's scheme *MoT-CCE* for cell-centered evolution and our new scheme *MoT-ICE* for interface-centered evolution.

For the *MoT-ICE*, we have proven uniform first- and second-order consistency. Initial numerical experiments confirm second-order accuracy for smooth solutions and high-resolution nonoscillatory shock-capturing properties for discontinuous solutions. The new scheme produces excellent radially symmetric solutions for a two-dimensional shallow-water explosion problem.

The main advantage of the *MoT-ICE-P1* seems to be its efficiency: it needs about the same cpu time as a second-order version of LeVeque's wave-propagation algorithm CLAWPACK, which, according to numbers given by Morel, is 4 to 5 times faster than the second-order-accurate *MoT-CCE-P1* developed by Fey, Jeltsch, and co-workers. This gain of efficiency is partly due to an improved second-order-accurate linerization and decomposition of the nonlinear system into advection equations and to the particularly simple characteristic transport algorithm for the resulting linear advection equations. This simplicity is retained in the case of three spatial dimensions.

In ongoing joint work with Christian von Törne, we are currently developing the *MoT-ICE* into a fully adaptive, distributed parallel code.

ACKNOWLEDGMENTS

The author thanks Michael Fey for generously sharing his insights into the Method of Transport and Christian von Törne for many stimulating discussions. The hospitality of Dr. Fey and Prof. Jeltsch and his group during visits at ETH Zürich is gratefully acknowledged. This work grew out of a joint research project funded by the German Science Foundation, Priority Research Program DFG-SPP ANumE.

REFERENCES

1. S. Billet and E. Toro, On WAF-type schemes for multidimensional hyperbolic conservation laws, *J. Comput. Phys.* **130**, 1 (1997).
2. B. Cockburn, F. Coquel, and P. LeFloch, Convergence of the finite volume method for multidimensional conservation laws, *SIAM J. Nurner. Anal.* **32**, 687 (1995).
3. P. Colella, Multidimensional upwind methods for hyperbolic conservation laws, *J. Comput. Phys.* **87**, 171 (1990).
4. M. Crandall and A. Majda, Monotone difference approximations for scalar conservation laws, *Math. Comput.* **34**, 1 (1980).
5. H. Deconinck, H. Paillère, R. Struijs, and P. Roe, Multidimensional upwind schemes based on fluctuation-splitting for systems of conservation laws, *Comput. Mech.* **11**, 323 (1993).
6. S. Deshpande, *A Second Order Accurate, Kinetic-Theory Based, Method for Inviscid Compressible Flows*, NASA Langley Technical Papers No. 2613, 1986.
7. M. Fey, *Ein echt mehrdimensionales Verfahren zur Lösung der Eulergleichungen*, dissertation, ETH Zürich Diss. No. 10034, 1993.

8. M. Fey, Multidimensional upwinding. I. The method of transport for solving the Euler equations, *J. Comput. Phys.* **143**, 159 (1998).
9. M. Fey, Multidimensional upwinding. II. Decomposition of the Euler equations into advection equations, *J. Comput. Phys.* **143**, 181 (1998).
10. M. Fey and R. Jeltsch, A simplified multidimensional Euler scheme, in *Proceedings of the First European Fluid Dynamics Conference, Brussels, Sept. 7–11, 1992*, edited by Ch. Hirsch (Elsevier, Amsterdam, 1992).
11. M. Fey, R. Jeltsch, J. Maurer, and A.-T. Morel, *The Method of Transport for Non-Linear Systems of Hyperbolic Conservation Laws in Several Space Dimensions*, Research Report No. 97-12, Seminar for Applied Mathematics, ETH Zürich, 1997.
12. M. Fey, R. Jeltsch, and A. Scascighini, *L^2-Stability of the Method of Transport for the 2-d Wave Equation*, Research Report, Seminar for Applied Mathematics, ETH Zürich, 1998.
13. S. Godunov, Finite difference methods for numerical computation of discontinuous solutions of the equations of fluid dynamics, *Math. Sb.* **47**, 271 (1959).
14. A. Harten and P. Lax, A random choice finite difference scheme for hyperbolic conservation laws, *SIAM J. Numer. Anal.* **18**, 289 (1981).
15. C. Hirsch, *Numerical Computation of Internal and External Flows* (Wiley-Interscience, New York, 1990), Vol. 2.
16. G.-S. Jiang and C.-W. Shu, Efficient implementation of weighted ENO schemes. *J. Comput. Phys.* **126**, 202 (1996).
17. D. Kröner, S. Noelle, and M. Rokyta, Convergence of higher order upwind finite volume schemes on unstructured grids for scalar conservation laws in several space dimensions, *Numer. Math.* **71**, 527 (1995).
18. J.-O. Langseth and R. LeVeque, *A Wave Propagation Method for Three-Dimensional Hyperbolic Problems*, preprint, 1995.
19. R. LeVeque, A large timestep generalization of Godunov's method for conservation laws, *SIAM J. Numer. Anal.* **22**, 1051 (1985).
20. R. LeVeque, CLAWPACK software, http://www.amath.washington.edu/rjl/clawpack.htlm.
21. R. J. LeVeque, Wave propagation algorithms for multidimensional hyperbolic systems, *J. Comput. Phys.* **131**, 327 (1997).
22. R. J. LeVeque and R. Walder, Grid alignment effects and rotated methods for computing complex flows in astrophysics, in *Proceedings of the Ninth GAMM Conference on Numerical Methods in Fluid Mechanics*, edited by J. B. Vos, A. Rizsi, and I. L. Rhyming, *Notes Numer. Fluid Mech.* **35**, 376 (1992).
23. X.-D. Liu, S. Osher, and T. Chan, Weighted essentially nonoscillatory schemes, *J. Comput. Phys.* **115**, 200 (1994).
24. M. Lukacova-Medvidova, K. Morton, and G. Warnecke, *Evolution Galerkin Methods for Hyperbolic Systems in Two Space Dimensions*, Report 97-44, Univ. Magdeburg, Germany, 1997.
25. J. Maurer, A genuinely multi-dimensional scheme for mixed hyperbolic-parabolic systems, in *Proceedings of the 7th International Conference on Hyperbolic Problems, Zürich, 1998*, edited by M. Fey and R. Jeltsch (Birkhäuser Basel, 1999), p. 713.
26. A.-T. Morel, *A Genuinely Multidimensional High-Resolution Scheme for the Shallow-Water* Equations, dissertation, ETH Zürich Diss. No. 11959, 1997.
27. S. Noelle, Hyperbolic systems of conservation laws, the Weyl equation, and multidimensional upwinding, *J. Comput. Phys.* **115**, 22 (1994).
28. S. Noelle, Convergence of higher order finite volume schemes on irregular grids, *Adv. Comput. Math.* **3**, 197 (1995).
29. S. Noelle, A note on entropy inequalities and error estimates for higher order accurate finite volume schemes on irregular families of grids, *Math. Comput.* **65**, 1155 (1996).
30. S. Noelle, The *MoT-ICE:* A new high-resolution wave-propagation algorithm based on Fey's Method of Transport, invited plenary lecture, in *Proceedings of the Second International Symposium on Finite Volumes for Complex Applications—Problems and Perspectives, Duisburg, Germany (July 1999)*, p. 95.
31. S. Ostkamp, Multidimensional characteristic Galerkin schemes and evolution operators for hyperbolic systems, *Math. Meth. Appl. Sci.* **20**, 1111 (1997).

32. M. Pandolfi and D. D'Ambrosio, Numerical instabilities in upwind methods: Analysis and cures for the "carbuncle" phenomenon, preprint, Polytecnico di Torino (1999) (submitted for publication).
33. B. Perthame, Second order Boltzmann schemes for compressible Euler equations in one and two variables, *SIAM J. Numer. Anal.* **29**, 1 (1992).
34. J. Quirk, A contribution to the Great Riemann Solver Debate, *Int. J. Numer. Meth. Fluid Dyn.* **18**, 555 (1994).
35. P. Roe, Approximate Riemann solvers, parameter vectors, and difference schemes, *J. Comput. Phys.* **43**, 357 (1981).
36. P. Roe, Discrete models for the numerical analysis of time-dependent multidimensional gas dynamics, *J. Comput. Phys.* **63**, 458 (1986).
37. P. Roe, Discontinuous solutions to hyperbolic systems under operator splitting, *Numer. Meth. Part. Diff. Eq.* **7**, 207 (1991).
38. P. Roe, Sonic flux formulae, *SIAM J. Sci. Stat. Comput.* **13**, 611 (1992).
39. R. Sanders and K. Prendergast, The possible relation of the 3-kiloparsec arm to explosions in the galactic nucleus, *Astrophys. J.* **188**, 489 (1974).
40. J. Steger and R. Warming, Flux vector splitting of the inviscid gas-dynamic equations with applications to finite difference methods, *J. Comput. Phys.* **40**, 263 (1981).
41. A. Szepessy, Convergence of a shock capturing streamline diffusion finite element method for a scalar conservation law in two space dimensions, *Math. Comput.* **53**, 527 (1989).
42. B. Van Leer, Towards the ultimate conservative difference scheme V, *J. Comput. Phys.* **32**, 101 (1979).
43. B. Van Leer, Flux vector splitting for the Euler equations, in *Proceedings of the 8th International Conference on Numerical Methods in Fluid Dynamics* (Springer-Verlag, Berlin/New York, 1982).
44. B. Van Leer, *Progress in Multi-Dimensional Upwinding*, ICASE Report 92-43 (1992).
45. R. Vilsmeier, F. Benkhallldoun, and D. Hänel, (editors), *Proceedings of the Second International Symposium on Finite Volumes for Complex Applications—Problems and Perspectives*, Duisburg, Germany, July 1999 (Hermes, Paris, 1999).
46. M. Westdickenberg and S. Noelle, A new convergence proof for finite volume schemes using the kinetic formulation of conservation laws. Accepted for publication.
47. K. Xu, *Gas Evoution Dynamics in Godunov-Type Schemes and Analysis of Numerical Shock Instability*, ICASE Report No. 99-6 (1999).
48. S. Zimmermann, The method of transport written as a kinetic scheme, in *Proceedings of the 7th International Conference on Hyperbolic Functions, Zürich, 1998*, edited by M. Fey and R. Jeltsch (Birkhäuser, Basel, 1999), p. 999.